Transient response of offshore wind turbines on monopiles in sand
Role of cyclic hydro-mechanical soil behaviour

Corciulo, Simone; Zanoli, Omar; Pisanò, Federico

Publication date
2017

Document Version
Final published version

Published in
Computers and Geotechnics

Citation (APA)
Corciulo, S., Zanoli, O., & Pisanò, F. (2017). Transient response of offshore wind turbines on monopiles in sand: Role of cyclic hydro-mechanical soil behaviour. *Computers and Geotechnics*, *83*, 221-238.

Computers and Geotechnics 83 (2017) 221–238

Contents lists available at ScienceDirect

Computers and Geotechnics

journal homepage: www.elsevier.com/locate/compgeo

Research Paper

Transient response of offshore wind turbines on monopiles in sand: role of cyclic hydro–mechanical soil behaviour

Simone Corciulo [a], Omar Zanoli [a], Federico Pisanò [b,*]

[a] D'Appolonia S.p.A. – Marine & Offshore Engineering, Via Martiri di Cefalonia 2, 20097 San Donato Milanese, Italy
[b] Geo-Engineering Section/Offshore Engineering Section, Delft University of Technology, Stevinweg 1, 2628 CN Delft, The Netherlands

ARTICLE INFO

Article history:
Received 9 June 2016
Received in revised form 14 November 2016
Accepted 16 November 2016

Keywords:
Offshore wind turbine
Monopile
Sand
Finite Element Method
Cyclic modelling
Hydro-mechanical coupling
Dynamic analysis

ABSTRACT

Offshore wind turbines (OWTs) in relatively shallow waters are most often founded on monopile foundations, whose design is extremely relevant to the OWT dynamic performance under environmental loading.

In this study, 3D finite element (FE) modelling is applied to the dynamic analysis of OWTs and proposed as a valuable support to current design practice. FE results are presented about the interplay of cyclic soil behaviour and hydro-mechanical coupling in determining the OWT natural frequency: in dilative sands, the natural frequency seems not to decrease monotonically at increasing loading amplitude, while slight influence of soil permeability is found.

1. Introduction

The gradual depletion of hydrocarbon reserves is currently pushing the energy market towards clean and sustainable sources, with solar and wind energies expected to play a major role in the coming decades. In this context, several European countries have been recently investing on the installation of offshore wind turbines (OWTs). According to the European Wind Energy Association (EWEA), Europe currently leads the offshore wind industry with a total offshore power capacity of 8 GW in 2014, to become 24 GW by 2020 and 66.5 GW by 2030 [28].

At present, most OWTs in Europe are supported by monopile foundations [4], open-ended steel tubes driven into the seabed by means of hydraulic hammers [22]. Large monopiles having 4–6 m diameter are routinely employed in relatively shallow waters (up to 30 m), while diameters close to 10 m are currently being considered for bigger 6–7 MW OWTs in water depths up to 60 m [22]. Monopile design is closely related to OWT dynamics, and in particular to the natural frequency f_0 associated with the first cantilever-like eigenmode. To avoid undesired resonance, OWTs are usually designed to keep f_0 within the $f_{1P} - f_{3P}$ range, where f_{1P} $(= 0.15 - 0.25$ Hz) is the rotor revolution frequency, while f_{3P} $(= 3f_{1P} = 0.45 - 0.75$ Hz for three-bladed OWTs) denotes the frequency of the aerodynamic pulses induced by the passage of the blades (*shadowing effect*). Setting $f_{1P} < f_0 < f_{3P}$ is commonly referred to as "soft–stiff" design, as it combines a stiff superstructure with a compliant (thus less expensive) foundation [44,79,6,18,41]. Profound understanding of dynamic soil–monopile interaction is therefore needed for an accurate evaluation of f_0.

In light of these premises, numerous research programmes have been recently carried out to improve the prediction of (i) soil–monopile lateral stiffness [15,42,6,49,18,77,78,10,85,11,3,80] and (ii) the displacements/rotations accumulated after thousands of loading cycles [2,48,7,74].

This paper targets a contribution to monopile design based on the modern feasibility of 3D finite element (FE) simulations, in agreement with the recent research agenda of the European Academy of Wind Energy (EAWE) [45]: "*what is the amount of soil damping for an offshore turbine? Is it possible to estimate soil damping from first principles, like from numerical simulation with solid elements?*" Despite the quite generic terminology, the EAWE agenda points out the relevance of dissipative phenomena (*damping*) and their 3D numerical simulation (via *solid elements*). Some of these issues have been previously addressed in the field of geotechnical earthquake engineering [43,86], such as the contemporary presence of (slow) dynamics, cyclic soil response and hydro-mechanical (HM) coupling. It seems thus sensible to reorient this existing knowledge towards OWT applications, as recently attempted by Cuéllar et al. [16].

* Corresponding author.
E-mail address: F.Pisano@tudelft.nl (F. Pisanò).

http://dx.doi.org/10.1016/j.compgeo.2016.11.010

The same modelling philosophy of Cuéllar et al. [16] is here extended to the integrated analysis of soil–monopile–OWT systems under environmental loading (wind and waves). In particular, the transient response of a standard 5 MW OWT is simulated to illustrate, under different loading scenarios, the interplay of cyclic loading and HM effects in determining f_0. The ultimate goal is to promote dynamic 3D HM FE calculations as a support to geotechnical design in offshore wind applications. It is shown that more advanced FE modelling may unravel important geotechnical aspects, possibly not emerging from standard analysis.

2. 3D FE modelling of soil–monopile–OWT systems

This section describes the main features of the soil–monopile–OWT FE model and refers to the most relevant background literature. The FE model has been set up through the OpenSees simulation platform (http://opensees.berkeley.edu, Mckenna [59] and Mazzoni et al. [56]), while the GID software [60] has been employed to post-process all numerical results. It is shown that soil–monopile interaction in OWTs can be naturally investigated within the same modelling framework already applied to seismically loaded piles [24,23,12,51].

2.1. Dynamic analysis of water-saturated soils

2.1.1. Governing equations

Based on the work by Zienkiewicz and coworkers [87,88,86], the so-called u–p formulation is here adopted to describe the dynamic HM response of the soil around the monopile. The u–p approach relies upon the assumption of negligible soil-fluid relative acceleration [87,50], which seems appropriate for offshore wind applications (wind/wave loading frequencies are normally lower than 0.5 Hz – see Sections 2.3 and 4.1).

2.1.2. FE solution

The u-p formulation leads to the following discrete system [88,37]:

mixture equilibrium :

$$\overbrace{\boldsymbol{M}\ddot{\mathbf{d}}}^{\text{mixture inertiae}} + \overbrace{\int_\Omega \boldsymbol{B}^T\boldsymbol{\sigma}'}^{\text{soil internal forces}} - \overbrace{\boldsymbol{Q}\boldsymbol{p}}^{\text{pore pressure forces}} = \overbrace{\boldsymbol{f}^{ext}_{u,\Gamma} + \boldsymbol{f}^{ext}_{u,\Omega}}^{\text{mixture external fluxes}}$$

water mass balance :

$$\overbrace{\boldsymbol{Q}^T\dot{\mathbf{d}}}^{\text{soil dilation/compaction}} + \overbrace{\boldsymbol{S}\dot{\mathbf{p}}}^{\text{fluid compressibility}} + \overbrace{\boldsymbol{H}\boldsymbol{p}}^{\text{seepage}} = \overbrace{\boldsymbol{f}^{ext}_{p,\Gamma} + \boldsymbol{f}^{ext}_{p,\Omega}}^{\text{fluid external fluxes}} \tag{1b}$$

based on the standard approximations $\mathbf{u} \approx \mathbf{N}_u\mathbf{d}$ and $p \approx \mathbf{N}_p\mathbf{p}$ for the displacement and the pore pressure fields, respectively (dots stand for time derivatives). If the interpolation functions in the arrays $\mathbf{N}_u$ and $\mathbf{N}_p$ do not fulfil the so-called *inf–sup* condition [5,9], then spurious pore pressure oscillations ("checkerboard" modes) may arise as the undrained-incompressible limit is approached [86,70,57,58]. This inconvenience is avoided here by resorting to the H1-P1ssp stabilised element formulation, recently proposed by McGann et al. [58] and applied for the first time to 3D OWT problems. Despite the low/equal order formulation, eight-node H1-P1ssp brick elements prove suitable against pressure oscillation owing to a non-residual–based stabilization [32], producing an additional Laplacian term in Eq. (1b) [58]:

$$\mathbf{Q}^T\dot{\mathbf{d}} + (\mathbf{S} + \tilde{\mathbf{H}})\dot{\mathbf{p}} + \mathbf{H}\mathbf{p} = \mathbf{f}^{ext}_{p,\Gamma} + \mathbf{f}^{ext}_{p,\Omega}$$
$$\text{where}: \quad \tilde{\mathbf{H}} = \sum_{\text{assemble}}^{m=1,N_{el}} \left(\int_{\Omega^e} \nabla\mathbf{N}_p^T \alpha \nabla\mathbf{N}_p d\Omega^{el} \right) \tag{2}$$

and preventing the well-known numerical issues associated with vanishing compressibility and permeability matrices ($\mathbf{S}$ and $\mathbf{H}$ in (1)). On the practical side, the value of the α coefficient in (2) governs the "amount of stabilisation" injected into system (1).[1] In what follows, the suggestion by McGann et al. [58] is taken as a reference:

$$\alpha = \frac{\alpha_0 h_{el}^2}{G_s + \frac{4}{3}K_s} \tag{3}$$

where h_{el} is, heuristically, the average element size within the FE mesh, G_s and K_s are the bulk and shear moduli of the soil skeleton, whilst α_0 is a scalar coefficient in the range of 0.1–0.5.

As for time integration, the well-known Newmark integration method is employed with parameters $\beta = 0.6$ and $\gamma = (\beta + 1/2)^2/4 = 0.3025$ [34]. Soil constitutive equations are integrated at Gauss points via the explicit forward Euler algorithm [76].

2.1.3. Cyclic sand modelling

The numerical analysis of environmentally loaded OWTs is strictly connected to the modelling of cyclic soil behaviour.[2] The present study relies upon the multi-surface plasticity model by Yang and Elgamal [83] (UCSD08 model), featuring: (i) non-linear hypoelastic law; (ii) frictional shear strength criterion with non-circular deviatoric π–section [46]; (iii) non-linear shear stress–strain response generated by multiple nested yield surfaces [64,71]; (iv) phase transformation line to distinguish dilative and compactive responses [36]; (v) ability to reproduce both liquefaction and cyclic mobility during undrained loading [84,26]. The interested reader is referred to Yang et al. [84], Elgamal et al. [26], Yang and Elgamal [83] for details on the model formulation and the calibration of constitutive parameters.

Unlike other cyclic models (see e.g. Dafalias and Manzari [17]), the UCSD08 formulation is not sensitive to variations in void ratio and cannot reproduce sand densification around the monopile [48,6]. However, densification effects are not deemed too relevant when the transient OWT response is analysed over relatively short loading events.

2.2. Monopile and superstructure

Elongated hollow structures may be idealised as general three-dimensional solids, cylindrical shells or beams. In this work, the superstructure (wind tower and transition piece) is modelled as a Timoshenko beam to account for combined bending and shear deformations [19]; conversely, the monopile is represented as a tubular 3D solid to reproduce genuine 3D effects in soil-structure interaction. In the same respect, one-phase 3D ssp bricks are preferred over shell elements for easier pre/post-processing procedures, especially when different solid formulations (one-phase and two-phase) coexist within the same OpenSees FE model. From the kinematic standpoint, the "mixed" structure formed by the 3D monopile and the OWT beam responds as a single Timoshenko beam, as long as rigid translational links are set between the OWT base and the monopile head.

Linear elastic behaviour is assumed for the whole steel structure, while 5% Rayleigh damping is set at 0.2 Hz and 8 Hz to generate low-frequency energy dissipation [13].

[1] Too low or high α will result in either ineffective or excessive stabilisation. Excessive stabilisation means an unrealistic/unphysical attenuation of the pore pressure field, due to the diffusive nature of the stabilising term (2).

[2] Reviews of the cyclic soil models proposed in the last decades are provided, for instance, by Prévost and Popescu [72], Zienkiewicz et al. [86], di Prisco and Wood [21], Pisanó and Jeremić [69].

2.3. Wind and wave loading

This section describes a simplified approach to create plausible wind/wave loading scenarios by assuming that: (i) wind and wave thrust forces on the OWT, F_{wind} and F_{wave}, depend mainly on the wind speed, the OWT geometry and certain empirical aero/hydro-dynamic factors; (ii) F_{wind} and F_{wave} are co-directional; (iii) the effect of rotor revolution on the wind speed around the OWT is negligible.

F_{wind} is evaluated through the so-called Blade Element Momentum (BEM) theory [62,47,54,53,55], regarding the rotor as a permeable actuator disc removing energy from a stream–tube-like wind flow. Simple considerations on fluid momentum and energy balance lead to the following wind thrust formula:

$$F_{wind}(t) = \frac{1}{2} A_{disc} C_T \rho_{air} V^2_{wind}(t) \tag{4}$$

where t is time, A_{disc} the area of the disc/rotor, $\rho_{air} = 1.2\ \mathrm{kg/m^3}$ the air density and $C_T = 0.688$ is an empirical wind thrust coefficient.

As for wave loading, F_{wave} is determined through the simplifying assumption of *fully developed sea*. Accordingly, the existence of an equilibrium sea state under a steady wind field is postulated, so that a wave power spectrum can be employed to quantify the wave energy S associated with each oscillation frequency f [68,30,66,33]. The single-parameter spectral formulation by Pierson and Moskowitz (PM spectrum) is adopted [68]:

$$S_{PM}(f) = \frac{\alpha g^2}{(2\pi f)^5} \exp\left[-\beta\left(\frac{g}{2\pi f V^{19.5\mathrm{m}}_{wind}}\right)^4\right] \tag{5}$$

where $\alpha = 0.0081$ and $\beta = 0.74$ are two dimensionless empirical factors, g the gravity acceleration and $V^{19.5\mathrm{m}}_{wind}$ the wind speed at 19.5 m above sea surface.[3] The wave frequency f_S at the maximum spectral amplitude and the corresponding wave height H_S can be easily derived as:

$$f_S^4 = \frac{4\beta}{5}\left(\frac{g}{2\pi V^{19.5\mathrm{m}}_{wind}}\right)^4 \qquad H_S = 2\sqrt{\frac{\alpha}{\beta}}\frac{\left(V^{19.5\mathrm{m}}_{wind}\right)^2}{g} \tag{6}$$

where H_S comes from the area under the $S_{PM}(f)$ spectral function. The f_S and H_S values in (6) define a simplified mono-harmonic sea state, and in turn the hydrodynamic thrust F_{wave} via the well-known Morison equation [63,81]. This latter relates the drag and inertial components of the wave thrust, F^D_{wave} and F^I_{wave}, to the tower diameter D, the water depth d, the wave height H_S and the peak frequency f_S:

$$\begin{aligned} F^D_{wave} &= \rho_w g \frac{C_d D}{8} H_{S2}\left(\frac{1}{2} + \frac{kd}{\sinh 2kd}\right) \\ F^I_{wave} &= \rho_w g \frac{C_m \pi D^2}{8} H_S \tanh kd \end{aligned} \tag{7}$$

Similarly, the overturning drag and inertial moments with respect to the mudline read as:

$$\begin{aligned} M^D_{wave} &= \rho_w g \frac{C_d D}{8} H_S^2 \left[\frac{d}{2} + \frac{2(kd)^2 + 1 - \cosh 2kd}{4k \sinh 2kd}\right] \\ M^I_{wave} &= \rho_w g \frac{C_m \pi D^2}{8} H_S d\left[\tanh kd + \frac{1}{kd}\left(\frac{1}{\cosh kd - 1}\right)\right] \end{aligned} \tag{8}$$

In Eqs. (7) and (8), ρ_w denotes the water density and k the wave number related to f_S, whereas $C_d = 0.65$ and $C_m = 1.6$ are the drag and inertia coefficients suggested by the American Petroleum Institute [40]. Since the drag and the inertial components of the wave force/moment are out of phase, the amplitudes of the force/moment resultants, F_{wave} and M_{wave}, are estimated via simplified SRSS averaging (Square Root of the Sum of the Squares). Finally, hydrodynamic loading can be globally represented as the following point load:

$$F_{wave}(t) = F_{wave}\sin(2\pi f_S t) = \sqrt{\left(F^D_{wave}\right)^2 + \left(F^I_{wave}\right)^2}\sin(2\pi f_S t) \tag{9}$$

applied at an elevation above the mudline equal to M_{wave}/F_{wave}.

[3] $V^{19.5\mathrm{m}}_{wind}$ can obtained from the anemometric value V_{wind} by assuming for the wind speed a power law (or more complicated) distribution along the elevation [66,31].

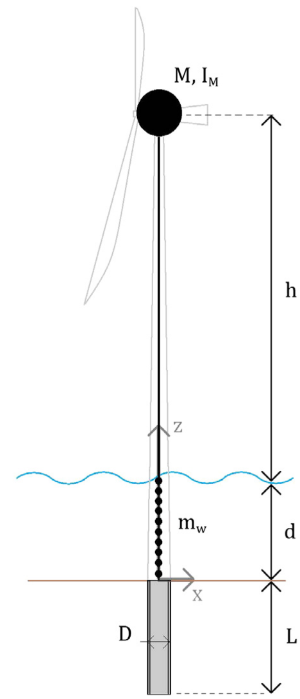

Fig. 1. The reference 5 MW OWT [39].

3. Model set-up and performance

3.1. Structural model

All FE results relate to the same 5 MW OWT, defined according to Jonkman et al. [39] and henceforth taken as a reference (Fig. 1). The dynamic analysis of the OWT-monopile steel structure requires the setting of (Table 1):

- the diameter D, the length L and the wall thickness t of the tubular monopile ($L/D = 4$ and $t/D = 0.01$ are considered here);
- the OWT elevation h above the sea level and the water depth d;
- the mass density ρ_s of steel and its elastic properties (Young's modulus E_s and Poisson's ratio ν_s);
- the cross–sectional properties of the OWT tower modelled as a Timoshenko beam (see Section 2.2), i.e. the section area A_{sec} and the moment of inertia I_{sec} with respect to the horizontal y axis. Constant A_{sec} and I_{sec} are assumed along the OWT tower;
- the inertial properties of the hub-nacelle assembly, including the total (lumped) mass M and the rotational inertia I_M associated with the nacelle mass imbalances in the xz plane;
- the sea water mass participating in the OWT vibration. Following Newman [65], this effect is incorporated by introducing an added water mass equal to:

$$m_w = 2\rho_w \frac{\pi D^2}{4} d \tag{10}$$

and evenly distributed along the underwater beam nodes of the OWT (Fig. 1).

Table 1
Geometrical and mechanical properties of the OWT–monopile structure.

h [m]	d [m]	L [m]	D [m]	t [cm]	ρ_s [ton/m^3]	E_s [GPa]	ν_s [–]	A_{sec} [m^2]	I_{sec} [m^4]	M [ton]	I_M [ton m^2]	m_w [ton]
90	20	20	5	5	7.85	200	0.3	0.7776	2.3818	350	2600	785

3.2. Soil parameters

The reference 5 MW OWT is assumed to interact with a homogeneous sand deposit. In order to generate a realistic soil response, the UCSD08 soil parameters have been calibrated against real laboratory test results, concerning a siliceous medium dense sand (relative density $D_R \approx 60\%$) from an offshore site in Myanmar (courtesy of D'Appolonia S.p.A.). The experimental tests were performed on sand specimens sampled at 20 m depth below the mudline, then subjected to anisotropic consolidation and triaxial shearing. Fig. 2 displays the comparison between experimental results and UCSD08 simulations for monotonic[4] (Fig. 2a–c) and cyclic[5] (Fig. 2d–f) undrained triaxial tests in terms of (i) effective stress path, (ii) stress–strain response and (iii) pore pressure evolution.

The UCSD08 parameters identified as suggested by Yang et al. [84] are listed in Table 2. The UCSD08 model can quite accurately reproduce the experimental test results, although the overpredicted accumulation of cyclic axial strain (*ratcheting*) should also be noticed (Fig. 2e). The latter is a genuine, poorly documented outcome of many existing cyclic models under non-symmetric load cycles [20,14].

The discontinuity in hydro-mechnical properties at the soil-monopile interface is handled according to the approach by Griffiths [29], i.e. by inserting a thin layer of solid (ssp) elements to model the physical transition from steel to soil. The interface layer is as thick as 4% of the monopile diameter and is assumed to behave as a UCSD08 saturated material. Specifically, the frictional angles mobilised at phase transformation and shear failure, ϕ_{PT} and ϕ', are set to 2/3 of the values in Table 2 to create a more deformable interface material.

3.3. Size and space discretization of the FE model

Appropriate size and space discretization for the soil FE domain around the monopile have been selected based on the preliminary tests documented in Appendix A. Fig. 3 illustrates the final soil domain discretised with approximately 6000 ssp bricks. Since only one lateral loading direction is considered (along the x axis in Fig. 3), geometrical and loading symmetries are exploited to reduce the high computational costs for 3D FE computations. The halved FE model features $Z/L = 1.5$, $W/L = 1.75$ and $W/D = 7$, with Z, W, L, D defined as in Fig. 3.

3.4. Loading stages and boundary conditions

All the numerical simulations are performed according to the following loading stages.

3.4.1. Soil gravity loading

At the very beginning, the FE model only includes soil elements (no structural members), initially at rest and unloaded. Then, the self-weight of the soil-water mixture is applied in increments to generate initial stress and pore pressure distributions. As for mechanical boundary conditions, the displacement components normal to the bottom and the lateral surfaces of the soil box in Fig. 3 are prevented, while the top surface is free. The same soil box is hydraulically impermeable along all its boundaries but at the top surface, where excess pore pressures are prevented.

3.4.2. OWT installation

The simulation of monopile installation procedures is not a goal of this work, where the traditional "wished-in-place" approach is conversely followed. The monopile-OWT structure is introduced into the FE model by removing two-phase soil elements in the pile zone and replacing them with mono-phase elements. In order to accommodate this replacement, the nodes at two-phase–mono-phase contact are duplicated and connected only through displacement components in a so-called "master-slave" fashion, automatically making the monopile surface impermeable to water flow. After the monopile is created, the above-mentioned rigid links between the pile head and the lower OWT nodes are introduced.

3.4.3. Transient analysis

The dynamic response of the soil-monopile-OWT system is finally simulated by modifying the above boundary conditions as follows:

1. the nodal fixities at the lateral/bottom surfaces of the soil domain are replaced by viscous dashpots[6] to damp out outgoing waves [52];
2. point forces at preselected nodes of the OWT beam are applied to model wind/wave loading.

As discussed in Appendix A, dynamic simulations are performed by setting the values $\Delta t = 0.004$ s and $\alpha = 6 \times 10^{-6}$ for the time step-size and the ssp stabilisation parameter in Eq. (3), respectively.

3.5. Features of soil-monopile-OWT dynamics

This section illustrates the predictive potential of the soil-monopile-OWT FE model. For this purpose, a point load is applied to the OWT hub (Fig. 4a) and the resulting transient response numerically simulated. The following loading time history is considered (Fig. 4b):

$$H(t) = \begin{cases} 0 \leqslant t \leqslant T_0: & H^{max}\sin(2\pi f t) \\ T_0 < t \leqslant T_f: & 0 \end{cases} \tag{11}$$

with $H^{max} = 1$ MN, $f = 0.5$ Hz, $T_0 = 8$ s and $T_f = 30$ s. All soil parameters are listed in Table 2.

3.5.1. HM soil response around the monopile

Variations in stresses, strains and pore water pressure are recorded in the FE soil domain while the OWT vibrates. The predicted excess pore pressure Δu is plotted against time in Fig. 5a–b for the four control points $A_{L,R}$ and $B_{L,R}$ (Fig. 4a); Fig. 5c–d illustrate normalised pore pressure isochrones for the three nodal columns in Fig. 4c at times t = 5, 10 s.

[4] the initial vertical (σ'_{v0}) and radial (σ'_{h0}) effective stresses equal 187 and 90 kPa, respectively, then axial loading is applied with a displacement rate equal to 0.02 mm/min.

[5] a ±140 kPa cyclic variation in vertical (total) stress is applied at 0.25 Hz starting from $\sigma'_{v0} = 155$ kPa and $\sigma'_{h0} = 60$ kPa.

[6] The viscous parameters of the boundary dashpots are set by accounting for the effect of water saturation on the propagation velocity of compressional P waves [27].

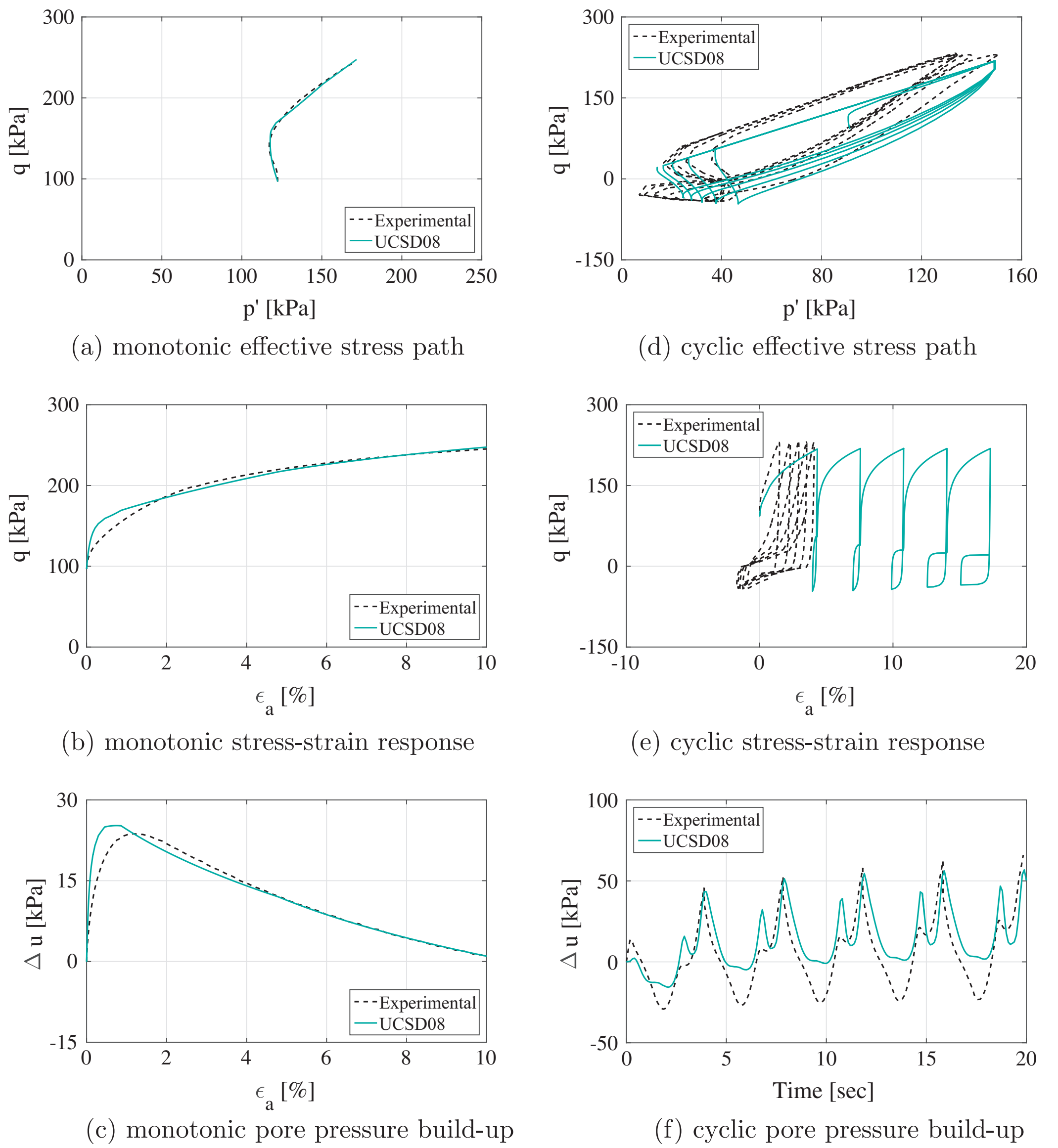

Fig. 2. Monotonic and cyclic triaxial response of medium dense sand specimens: comparison between experimental data (courtesy of D'Appolonia S.p.A) and UCSD08 simulations.

Table 2
HM soil parameters [83].

Parameter	Unit	Value
Reference shear modulus G_r	[kPa]	1×10^5
Reference bulk modulus K_r	[kPa]	1.7×10^5
Reference effective confinement p'_r	[kPa]	100
Pressure dependence coefficient n	[–]	0.5
Friction angle ϕ'	[deg]	35.5
Shear strain γ_{max} at peak strength	[–]	0.085
Phase transformation angle ϕ_{PT}	[deg]	31
Contraction parameter c_1	[–]	0.125
Contraction parameter c_2	[–]	0.5
Contraction parameter c_3	[–]	1
Dilation parameter d_1	[–]	0.25
Dilation parameter d_2	[–]	3.9
Dilation parameter d_3	[–]	5.7
Liquefaction strain parameter p'_y	[–]	1.95
Liquefaction strain parameter $\gamma_{s_{max}}$	[–]	0
Saturated mass density ρ	[ton/m^3]	1.8
Darcy permeability k	[m/s]	5×10^{-4}

At the considered locations, Δu evolves in time depending on (i) variations in total mean stress p, (ii) water drainage (drained, partially drained or undrained response) and (iii) soil volume changes under shear loading. In particular, the results in Fig. 5 suggest that:

– the sign of the excess pore pressure is mostly governed by the current position of the vibrating monopile. Under "passive-like" conditions (the pile is intruding into the soil), the total mean confinement tends to increase and positive Δu arises. At the same time, negative Δu is recorded on the opposite side of the monopile ("active-like" conditions);
– the portion of Δu induced by volumetric-deviatoric coupling is typically negative in medium dense sands (Section 3.2). Therefore, the two interplaying pressure generation mechanisms give rise to Δu oscillations with more pronounced negative peaks.
– pressure isochrone patterns evolve as the OWT transits from forced ($t \leqslant T_0$) to free/damped ($t > T_0$) vibration. The smooth pressure isochrones testify the effectiveness of the ssp stabilisation [58].

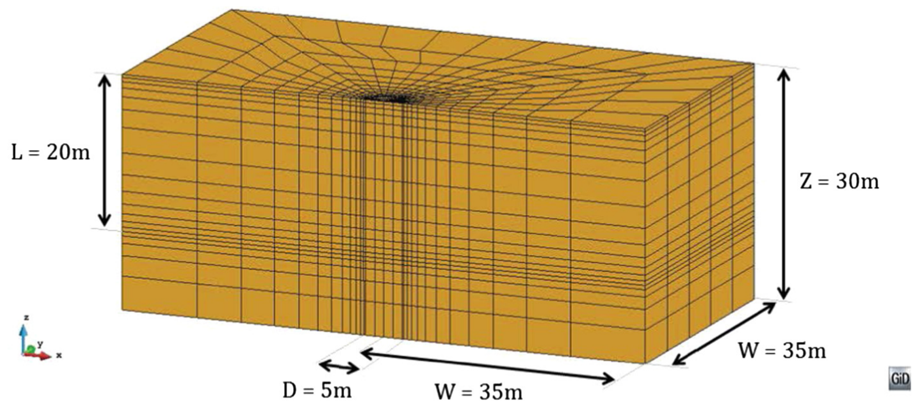

Fig. 3. Soil domain and ssp FE discretisation.

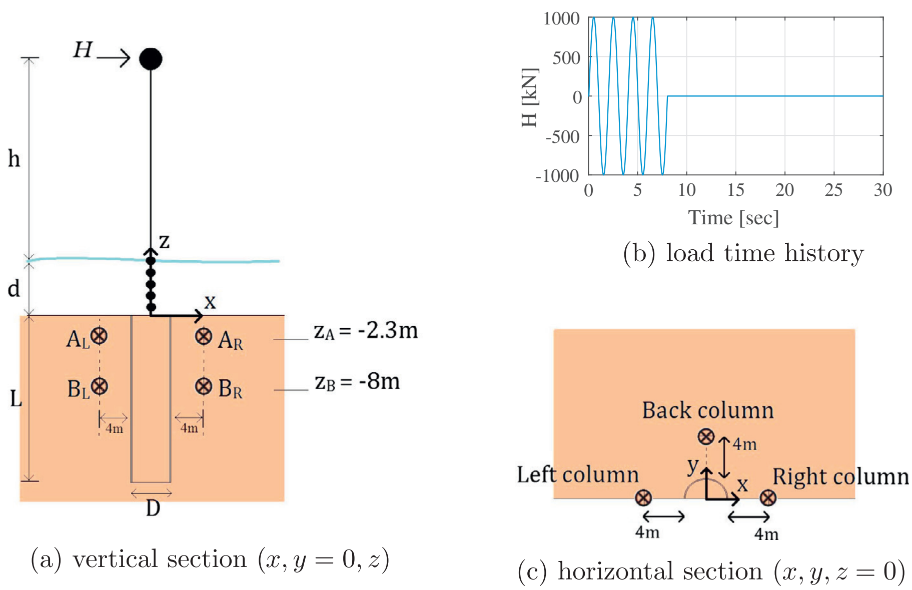

Fig. 4. Point-loaded OWT and control locations defined for plotting purposes.

The pore pressure evolution is obviously linked to the mechanical response of the soil, here represented in terms of shear stress-strain curves (Fig. 6) and effective stress paths (Fig. 7) at points $A_{L,R}$ and $B_{L,R}$. If the $\tau_{xz} - p'$ stress paths cross the phase transformation line during shear loading, then the effective mean pressure p' increases due to negative excess pore pressure and, as a consequence, higher shear stresses can be borne by the soil. This contradicts a common misconception: soil non-linearity does not always imply softer response and lower strength, but the opposite may be true in presence of dilative granular materials.

3.5.2. Vibrational response of the monopile-OWT structure

The dynamic response of the monopile-OWT structure is visualised in Fig. 8 in both time and frequency domains. The displacement time histories simulated at the OWT hub and monopile head are plotted in Fig. 8a–b. While the monopile head displaces much less than the hub, the comparison to the hub response predicted by a simpler clamped OWT model (grey line) points out the quantitative significance of the foundational compliance.

The frequency domain performance is shown in Fig. 8c in terms of numerical frequency response function (FRF) at the OWT hub mass (Fourier amplitude ratio between the inertia force – mass times acceleration – and the input load). The numerical FRF (blue[7] solid line) is also interpolated with the analytical FRF of a visco-elastic single-degree-of-freedom (1DOF) oscillator (grey dashed line):

$$FRF = \frac{1}{\sqrt{(1 - f/f_0)^2 + (2\xi f/f_0)^2}} \tag{12}$$

where f_0 denotes the natural frequency and ξ the damping ratio [13]. Although the analytical–numerical comparison is only reliable around f_0,[8] realistic natural frequency and damping ratio are estimated – 0.243 Hz and 6.5%, respectively. ξ is correctly larger than the 5% value set for the OWT beam (Section 2.2), as it also includes the energy dissipation due to soil plasticity and wave radiation.

3.6. Role of the soil volumetric behaviour

The results of a purely numerical experiment are reported to stress the structural implications of the soil volumetric behaviour. For this purpose, the UCSD08 model is first recalibrated by keeping the parameters in Table 2 and resetting $\phi_{PT} = \phi'$. Fig. 9a displays

[7] For interpretation of color in 'Figs. 8 and 9', the reader is referred to the web version of this article.

[8] Numerical spectral ratios are meaningless at frequencies associated with negligible input spectral amplitudes – in Fig. 8c, at frequencies out of the 0.2–0.3 Hz range.

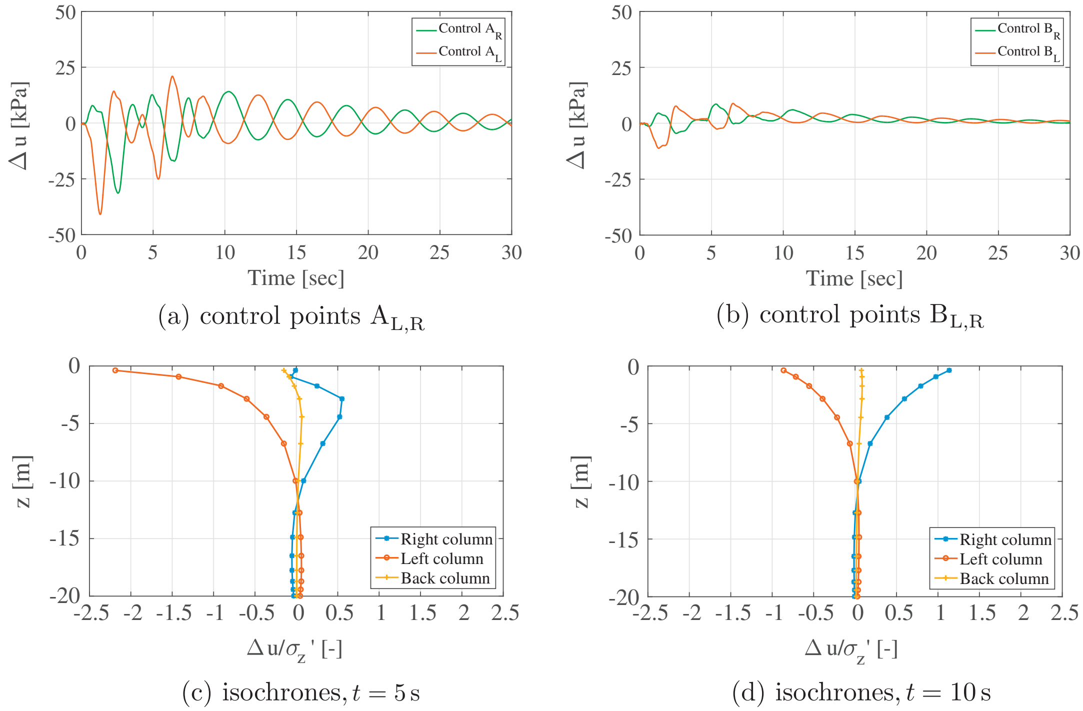

Fig. 5. Time evolution and isochrones of excess pore pressure at the locations in Fig. 4.

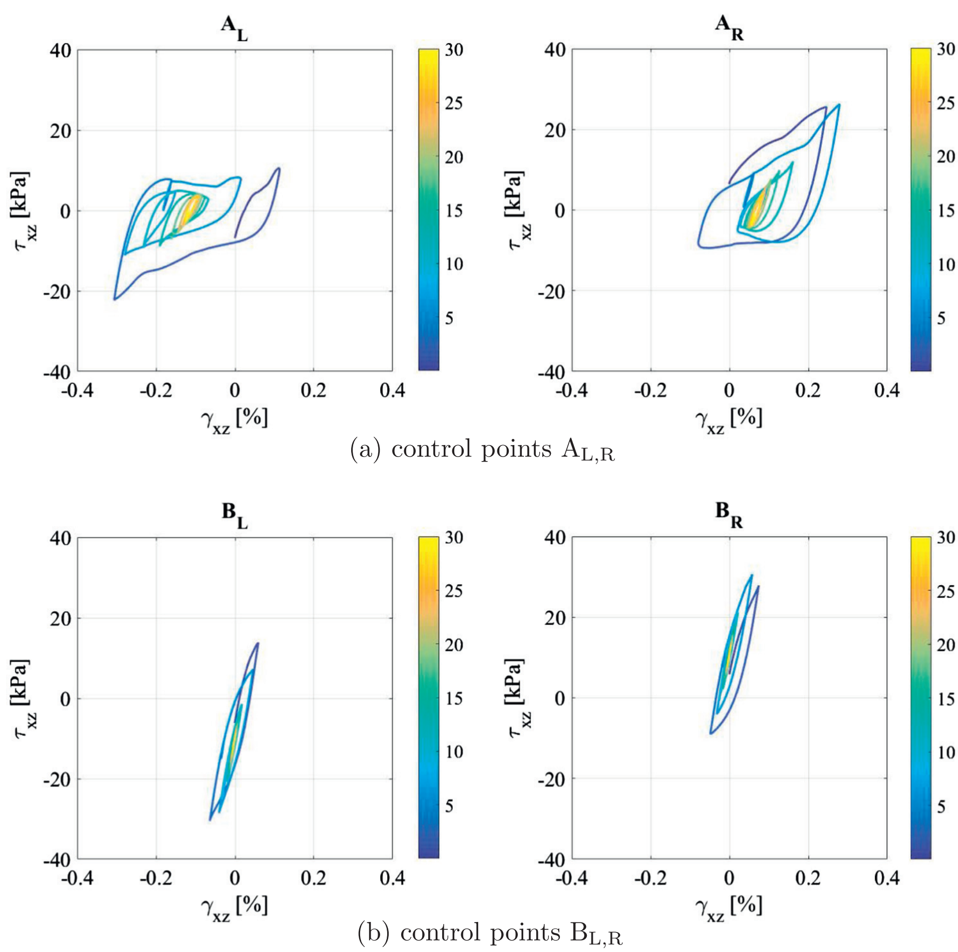

Fig. 6. Shear stress–strain response at the control points defined in Fig. 4. The colorbars indicate the time elapsing from 0 to 30 s. (For interpretation of the references to color in this figure legend, the reader is referred to the web version of this article.)

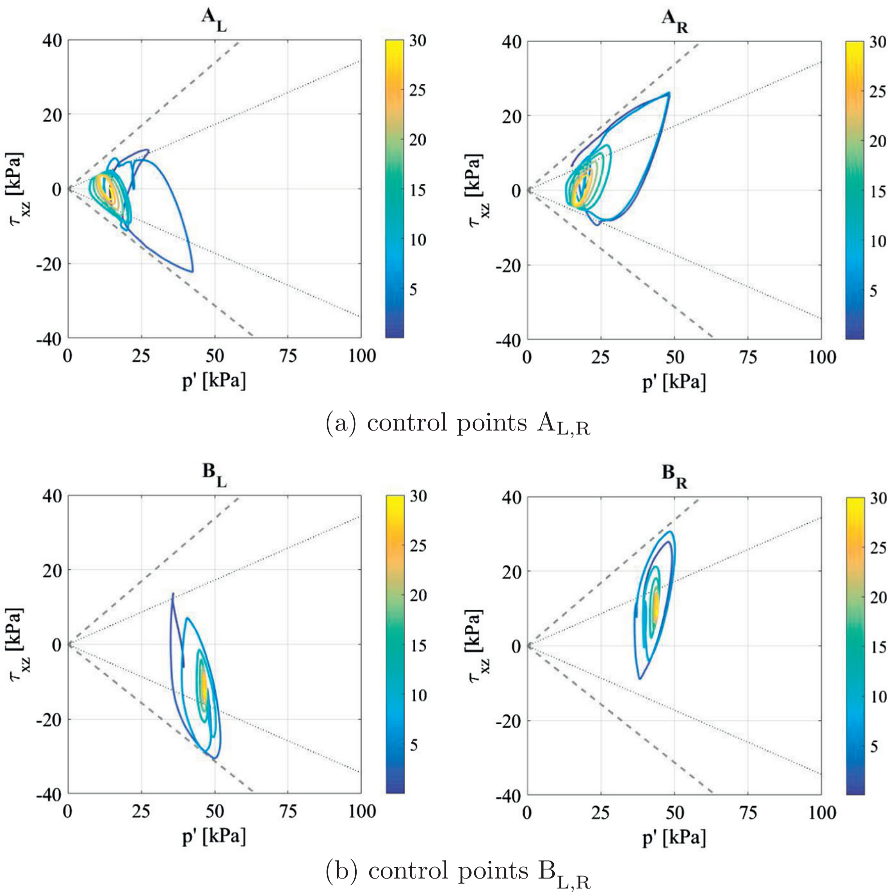

(a) control points $A_{L,R}$

(b) control points $B_{L,R}$

Fig. 7. Effective stress paths at the control points defined in Fig. 4. Failure (dashed lines) and phase transformation (dotted lines) loci are also plotted. The colorbars indicate the time elapsing from 0 to 30 s. (For interpretation of the references to color in this figure legend, the reader is referred to the web version of this article.)

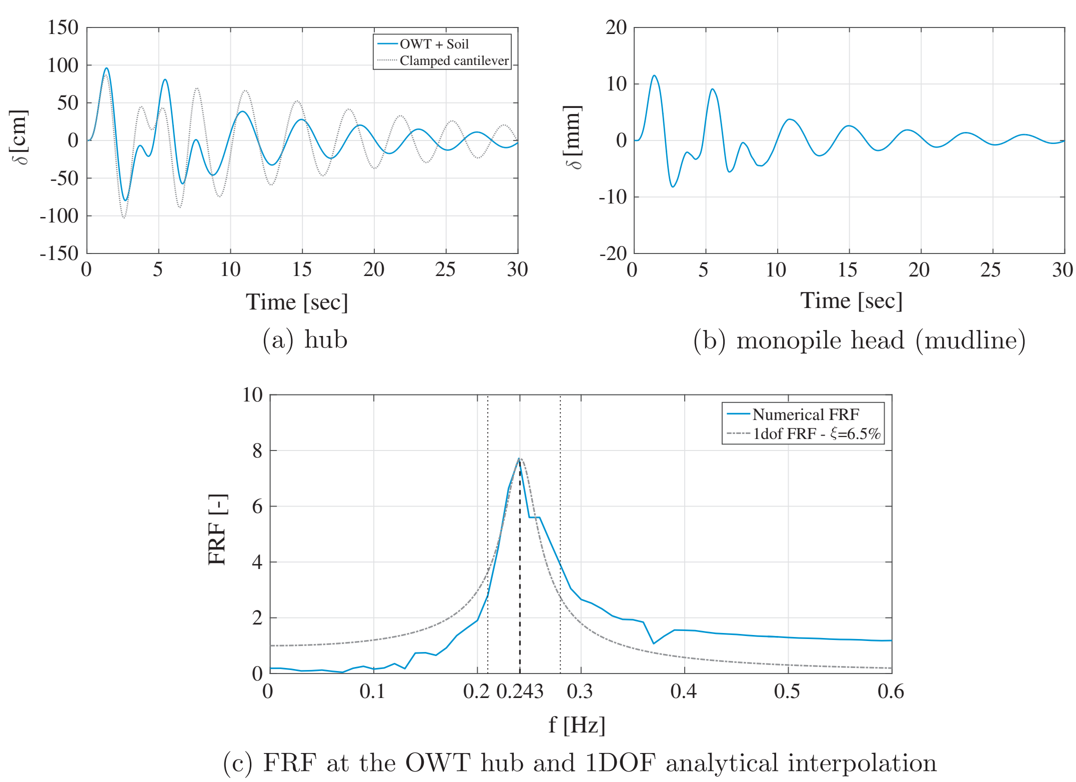

(a) hub

(b) monopile head (mudline)

(c) FRF at the OWT hub and 1DOF analytical interpolation

Fig. 8. Dynamic response of the monopile-OWT structure.

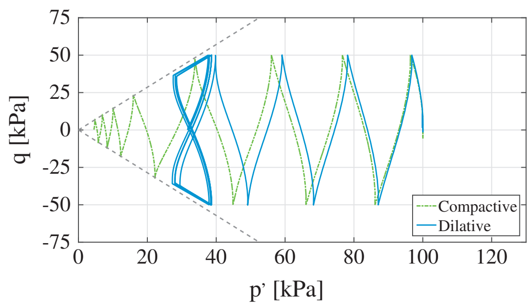

(a) dilative and compactive calibrations of the UCSD08 flow rule

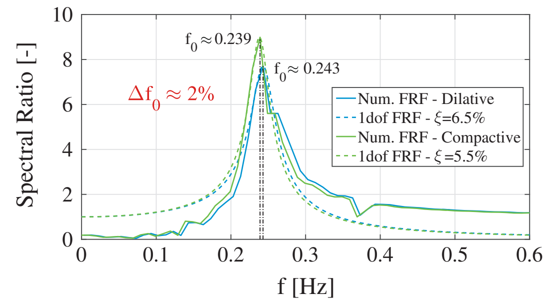

(b) numerical FRFs and 1DOF interpolations

Fig. 9. Relation between soil volume changes and OWT dynamics: dilative vs compactive plastic flow rules.

the effect of this recalibration in terms of undrained soil response to symmetric triaxial loading: while the previous parameter calibration gave rise to the typical behaviour of dilative sands (blue line), the new calibration results in a liquefying response (green line).

Fig. 9b illustrates the FRFs obtained for two identical OWTs, one funded in the dilative sand and the other in its "virtual" compactive counterpart. The transition from dilative to compactive sand behaviour is itself responsible for a 2% reduction in f_0 (from 0.243 Hz to 0.239 Hz), not negligible in the context of offshore wind applications. As discussed in different research contexts [35,25,8,73], soil dilation can give rise to stiffer soil responses under both undrained and drained conditions: in the former case, the development of negative excess pore pressure enhances the effective confinement around the monopile; in the latter, higher confining stresses result from prevented volume expansion.

4. OWT response to environmental loading

The OWT response to more realistic environmental loading is discussed in the following. Structural specifications, soil properties and analysis parameters are as in the previous sections.

4.1. Loading scenarios

The wind/wave thrust forces depicted in Fig. 10 are determined as described in Section 2.3. For this purpose, four different anemometric records are considered to represent typical wind conditions in the Irish Sea (courtesy of Siemens Wind Power). Four realistic loading scenarios – corresponding to average wind speeds V^{avg}_{wind} of approximately 5, 10, 15, 20 m/s (cases A, B, C, D) – are generated as follows:

1. wind velocity records (total duration: 600 s) are first reduced to 30 s time histories for computational convenience. Then, wind velocities are directly converted into wind thrust forces via the BEM Eq. (4);
2. the PM wave spectrum is computed for the considered OWT structure and water depth (Fig. 10), then the main wave frequency f_S and the corresponding wave height H_S are obtained. For given f_S, H_S and structural specifications, the wave thrust forces and their application points $\delta_{F_{wave}}$ (elevation with respect to the mudline) are determined through Eqs. (7) and (8).

The resulting wind/wave load histories are plotted in Fig. 11, while the corresponding load parameters are listed in Table 3. As can be noted, wind and wave forces are gradually applied through a 5 s ramp to avoid failure of FE simulations due to sudden load application.

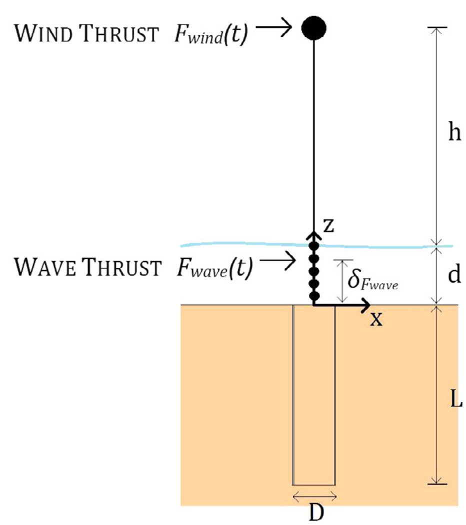

Fig. 10. OWT subjected to wind/wave point loads.

4.2. Numerical results

The main numerical outcomes are illustrated for the above loading cases in terms of soil–monopile interaction (Section 4.2.1) and OWT dynamics (Section 4.2.2). For all V^{avg}_{wind} scenarios, the soil permeability is gradually varied in order of magnitude within the $10^{-2} - 10^{-7}$ m/s range (k values are thus regularly spaced on a logarithmic scale).

4.2.1. Soil–monopile interaction

Fig. 12 shows the simulated displacement response of the monopile head at varying soil permeability. The maximum displacement – and its unrecoverable component – increases substantially at larger V^{avg}_{wind}, with higher pile deflections predicted as the drained limit is approached ($k \to 10^{-2}$ m/s). While the prevention of soil volume changes is expected to affect the monopile displacements, soil permeability does not seem to influence the oscillation frequency at the monopile head. It should be also noted that the transition from the undrained to the drained limit is affected by V^{avg}_{wind}: as more soil non-linearity is mobilised at increasing V^{avg}_{wind}, higher permeabilities are needed for a fully drained response.

Fig. 13 highlights the relationship between soil strains and V^{avg}_{wind}. The deviatoric strain patterns around the monopile suggest that severe soil strains (larger than 0.1%) may not arise when $V^{avg}_{wind} < 10$ m/s. Further, although significant plastic straining

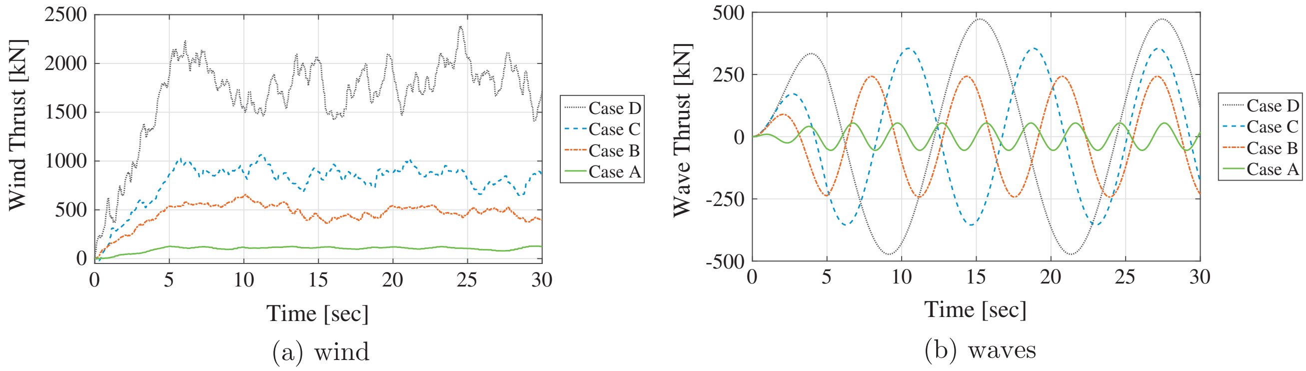

Fig. 11. Wind/wave thrust time histories.

Table 3
Wind/wave load specifications for the four wind speed scenarios.

	V_{wind}^{avg} [m/s]	F_{wind}^{avg} [kN]	f_S [Hz]	H_S [m]	F_{wave}^{max} [kN]	$\delta_{F_{wave}}$ [m]
Case *A*	4.83	109	0.336	0.36	±55	17.8
Case *B*	10.34	500	0.157	1.64	±243	12.3
Case *C*	13.56	860	0.120	2.81	±355	11.0
Case *D*	19.76	1820	0.082	5.97	±473	10.3

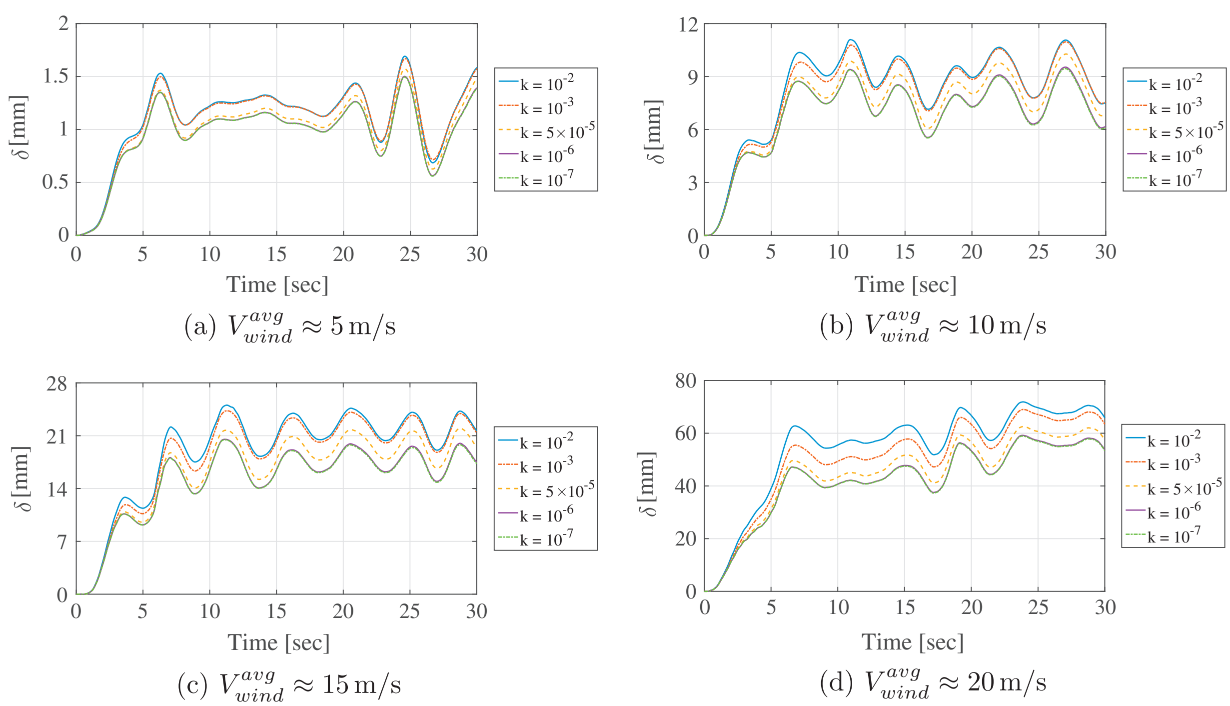

Fig. 12. Displacement response of the monopile head (mudline) at varying soil permeability k [m/s].

occurs at the largest load amplitude ($V_{wind}^{avg} \approx 20$ m/s), only a small amount of the total lateral capacity is mobilised. This is clearly illustrated in Fig. 14, where the shear force time history at the monopile head (Fig. 14a) is compared to the lateral load-displacement curve obtained through static pushover (solid line in Fig. 14b). For verification purposes, the simulated lateral response is plotted along with the stiffer curve obtained by Abdel-Rahman and Achmus [1] for a larger monopile ($D = 7.5$ m and same length $L = 20$ m).

4.2.2. OWT natural frequency

Fig. 15 shows the displacement response of the OWT hub to the load scenarios A, B, C and D at varying permeability; the results are also compared to the predictions for an OWT clamped at the mudline (grey lines). As observed in Fig. 8a, the presence of a compliant foundation affects significantly the global response and the natural frequency. On the other hand, soil permeability seems to negligibly impact the hub displacement (in the order of tens of centimeters), even though its influence has been clearly observed at the mono-

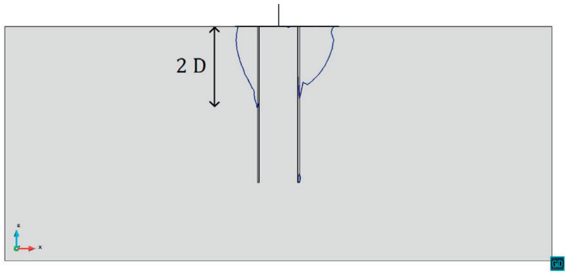

(a) $V_{wind}^{avg} \approx 10\,\mathrm{m/s}$, vertical

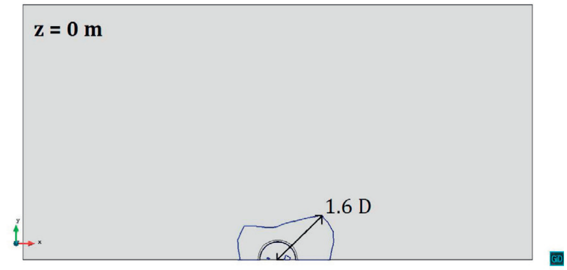

(b) $V_{wind}^{avg} \approx 10\,\mathrm{m/s}$, horizontal

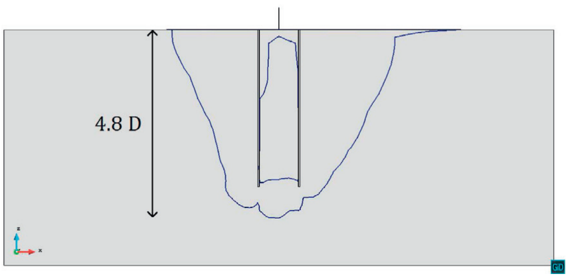

(c) $V_{wind}^{avg} \approx 20\,\mathrm{m/s}$, vertical

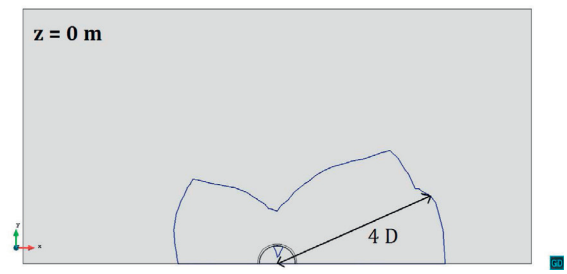

(d) $V_{wind}^{avg} \approx 20\,\mathrm{m/s}$, horizontal

Fig. 13. 0.1% deviatoric strain contour lines – vertical $(x, y = 0, z)$ and horizontal $(x, y, z = 0$ – mudline) sections (soil permeability: $k = 10^{-6}$ m/s).

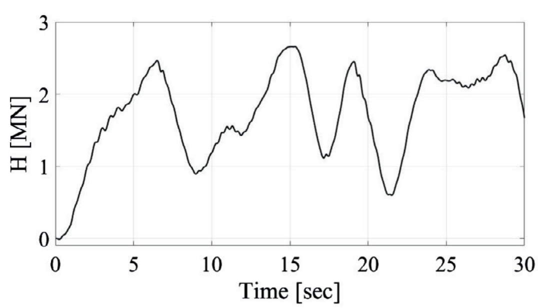

(a) shear force time history

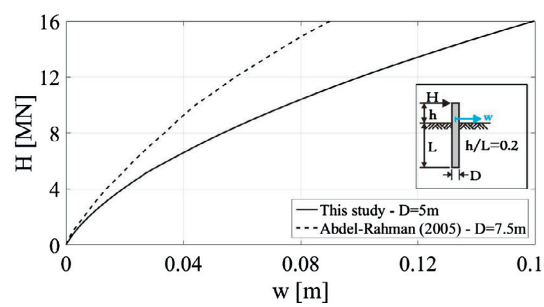

(b) lateral load-displacement curve (comparison with Abdel-Rahman and Achmus (2005))

Fig. 14. Lateral response of the monopile head at $V_{wind}^{avg} \approx 20\,\mathrm{m/s}$.

pile head for medium-large wind speeds (Fig. 12). These two observations are not in contradiction after considering the 100 m distance between the mudline and the OWT hub: the magnitude of the OWT displacement is dominated by the structural flexibility, so that relatively slight variations in monopile deflection do not produce severe effects at the top of the wind tower.

The same inference is supported by Fig. 16, where the power spectral density (PSD) of the hub displacement is plotted after normalisation by the maximum value $(0 \leqslant PSD \leqslant 1)$ – the spectral peaks $(PSD = 1)$ identify the OWT natural frequency f_0. f_0 is compared in Fig. 16 to the natural frequencies computed for (i) clamped OWT (circular marker) and (ii) OWT in linear elastic soil[9] (square marker). Unlike the clamped and the linear elastic f_0 values, the "non-linear" natural frequency varies in relation to the load amplitude (V_{win}^{avg}) and the following features of sand behaviour: (i) sand stiffness increases at larger effective confinement p'; (ii) sand stiffness decreases under shear straining; (iii) volume HM effects in dilative sands result in higher shear stiffness. In light of these observations, it is possible to explain the observed variations in f_0:

(a) $V_{wind}^{avg} \approx 5$ m/s – low soil plasticity is mobilised, so that the global response is mostly non-linear elastic. The local variations in effective confinement make the sand stiffer than it is immediately after gravity loading (Section 3.4), and f_0 gets closer to the clamped value;
(b) $V_{wind}^{avg} \approx 10$ m/s – as the load amplitude increases, deviatoric straining implies lower sand stiffness and f_0;
(c) $V_{wind}^{avg} \approx 15$ m/s – the soil shear stiffness and f_0 keep decreasing;
(d) $V_{wind}^{avg} \approx 20$ m/s – substantial soil plasticity and HM volume effects are triggered. In dilative sands, these are expected to stiffen the soil, and indeed a slight increase in f_0 is noted. This finding confirms what inferred from Fig. 9.

[9] The linear elastic f_0 has been determined by inhibiting soil plastic strains and recording the OWT free vibrations induced by a very small initial load (10 kN, not inducing substantial variations in the soil elastic moduli).

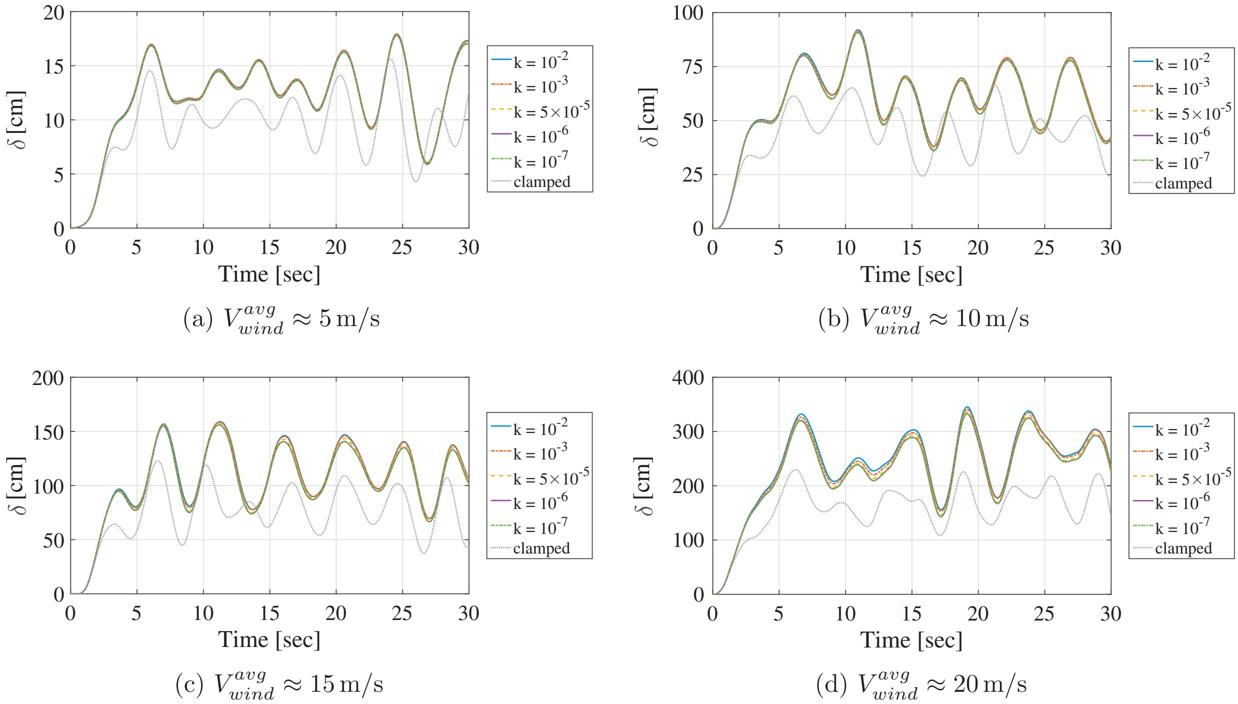

Fig. 15. Displacement response of the OWT hub at varying soil permeability k [m/s].

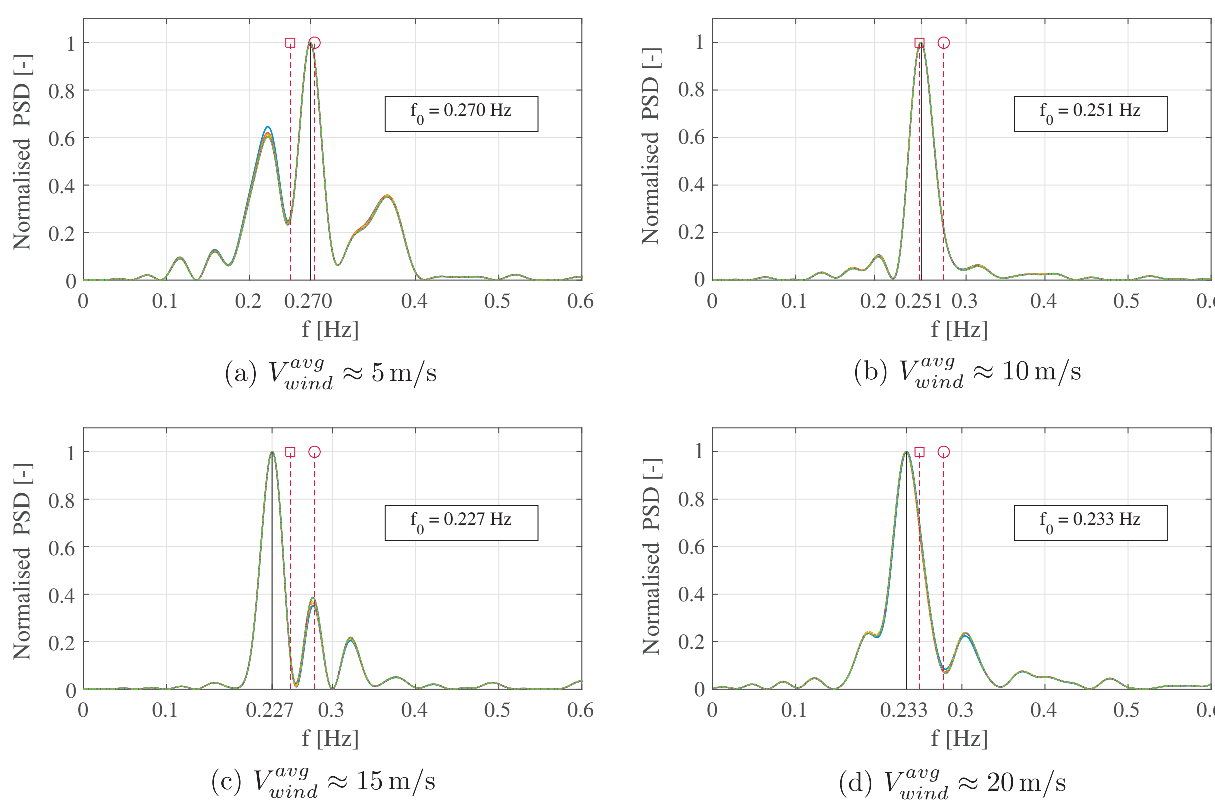

Fig. 16. Normalised displacement power spectra for the OWT hub at varying soil permeability. The circular and the square markers denote the f_0 associated with a clamped OWT and an OWT in a linear elastic sand, respectively.

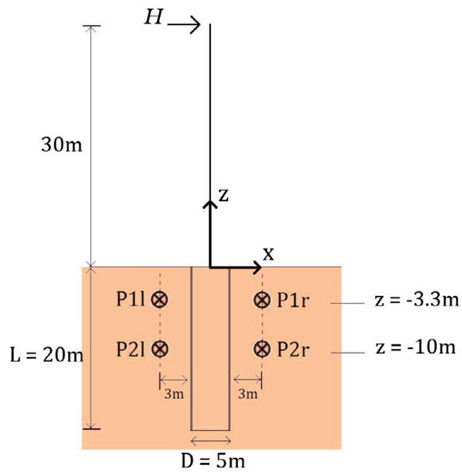

(a) geometrical specifications

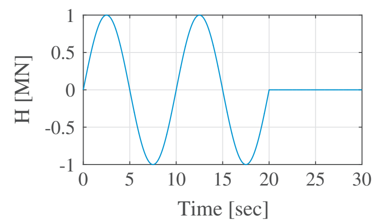

(b) load time history

Fig. 17. Reference analysis case.

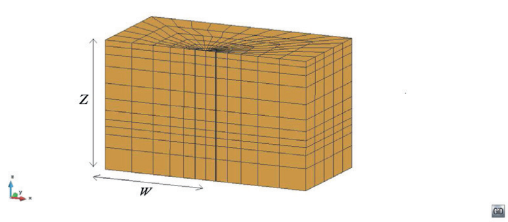

(a) Mesh A: $Z = 30\,\mathrm{m}$, $W = 25\,\mathrm{m}$

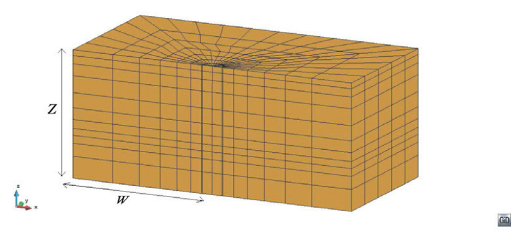

(b) Mesh B: $Z = 30\,\mathrm{m}$, $W = 35\,\mathrm{m}$

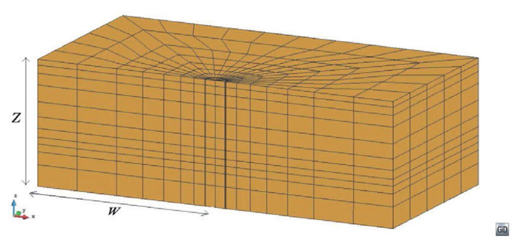

(c) Mesh C: $Z = 30\,\mathrm{m}$, $W = 45\,\mathrm{m}$

Fig. 18. FE meshes employed for domain size sensitivity analysis.

5. Concluding remarks

A 3D HM FE model was developed for the time-domain analysis of environmentally loaded OWTs, accounting for (i) slow soil dynamics, (ii) pore pressure effects and (iii) non-linear cyclic soil behaviour. Specifically, the well-known u-p formulation was adopted in combination with the UCSD08 soil model, while the computational efficiency was globally enhanced by exploiting the very recent equal-order H1-P1ssp element formulation.

A standard 5 MW OWT was analysed under four wind speed scenarios ($V_{wind}^{avg} \approx 5, 10, 15, 20\,\mathrm{m/s}$) and with soil permeability varying from 10^{-2} m/s to 10^{-7} m/s. Although real site conditions (e.g. in the North Sea) would include stratigraphic inhomogeneity, a typical 5 MW OWT in a homogeneous medium dense sand layer was considered. The numerical results allowed to gain insight into some relevant geotechnical aspects:

– soil non-linearities may become particularly influential at wind speeds larger than 10 m/s;
– at medium-large loading levels, the pore pressure regime has clear influence on monopile displacements, but negligibly affects the OWT response at the hub (and therefore the natural frequency);
– the OWT natural frequency results from the complex interplay of loading amplitude and non-linear/dilatancy effects in the soil. More soil non-linearity does not necessarily imply a monotonic decrease of the natural frequency.

Future developments along this research line will aim to improve model reliability in terms of (i) cyclic soil modelling (void ratios effects and ratcheting), (ii) site inhomogeneity (layering) and (iii) environmental loading (longer time histories and more complex loading combinations). The goal is to keep providing more solid ground for reviewing current design methods on the basis of integrated FE modelling.

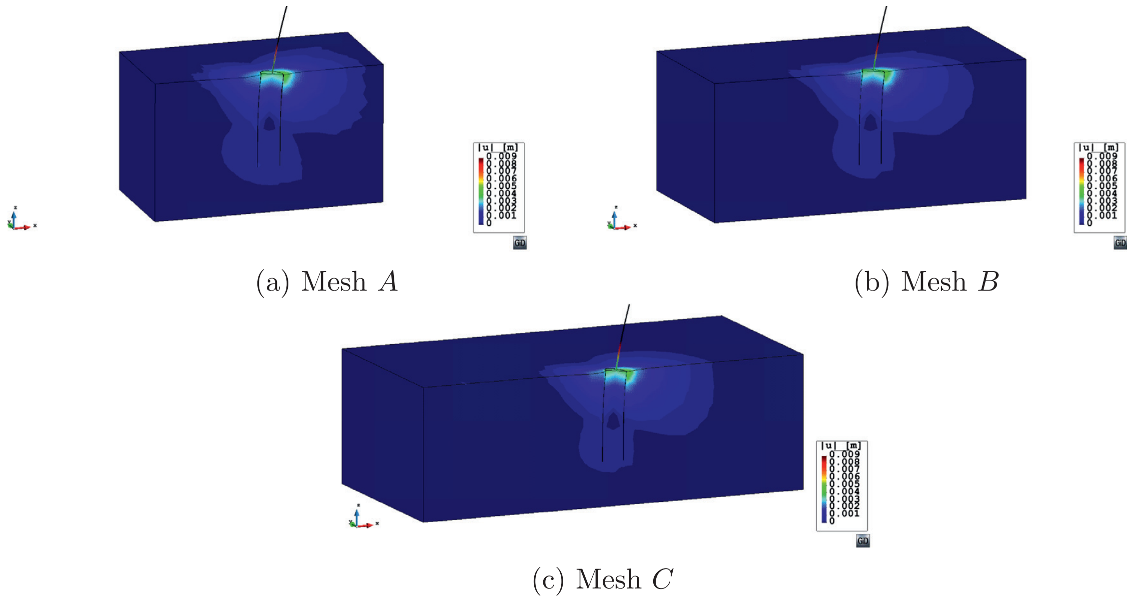

Fig. 19. Domain size sensitivity analysis: total displacement norm at the second positive load peak (Fig. 4b).

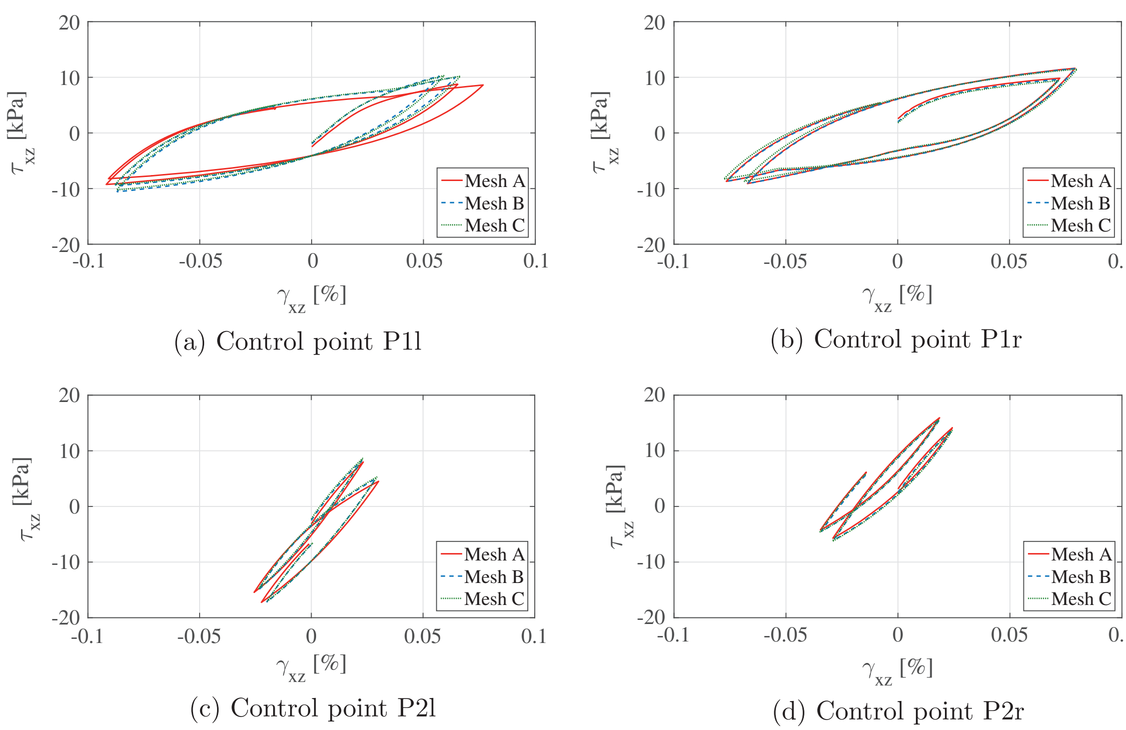

Fig. 20. Domain size sensitivity analysis: $\tau_{xz} - \gamma_{xz}$ cycles at the four control points in Fig. 17b.

Acknowledgements

D'Appolonia S.p.A (San Donato Milanese, Italy) and Siemens Wind Power (The Hague, The Netherlands) are gratefully acknowledged for providing real data from laboratory soil tests and anemometric measurements, respectively. Warm thanks also go to Pim Versteijlen (TU Delft/Siemens Wind Power) and Frank Renting (TU Delft) for their useful suggestions on the modelling of OWT structures and environmental loads.

Appendix A. Sensitivity of FE results to model set-up

In this appendix, preliminary results about the setting of model size, space/time discretization and pore pressure stabilization are summarised.

A.1. Domain size

The role played by the FE domain size is illustrated with reference to the analysis case in Fig. 17. A 5 m diameter monopile is connected to a 30 m beam, loaded at the top by a sinusoidal force (frequency $f = 0.1$ Hz, amplitude $H^{max} = 1$ MN). All monopile specifications and soil parameters are as in Tables 1 and 2 (except soil permeability, $k = 10^{-6}$ m/s), with structure elevation equal to 30 m and no additional lumped masses. Three relatively coarse meshes, A, B and C, are first tested to explore domain size effects (Fig. 18 – in all cases, the same size W is kept along the x and y directions). The corresponding FE results are reported in Figs. 19 and 20 in terms of (i) contour plots of total displacement norm and (ii) shear stress-strain response ($\tau_{xz} - \gamma_{xz}$) at the four control points in Fig. 17.

While the contour plots in Fig. 19 indicate the insufficient size of mesh A (non-negligible displacements are recorded close to the outer boundaries), mesh B and C provide very similar results in terms of both displacement norm and stress-strain cycles. The size of mesh B seems thus appropriate, as well as in good agreement with the previous size settings by Cuéllar et al. [16].

A.2. Space/time discretization

The sensitivity to space discretization is investigated starting from the above mesh B, then renamed B1 and further refined. The gradual mesh refinement is illustrated in Fig. 21 for the three meshes B1, B2, B3, formed by approximately 3000, 6000 and 8000 ssp elements. The analysis case in Fig. 17 is numerically studied in combination with the three meshes above, and the corresponding results plotted in Fig. 22 (contour plots of excess pore pressure Δu) and Fig. 23 ($\tau_{xz} - \gamma_{xz}$ cycles at the four control points in Fig. 17).

In this case, the influence on the excess pore pressure field does not seem dramatic, while substantial mesh effects are visible in the shear stress-strain response at points P1l and P1r. The medium mesh B2 seems a reasonable compromise between accuracy and computational costs – the latter significantly increase for mesh B3. Further, mesh B2 compares well with the space discretization

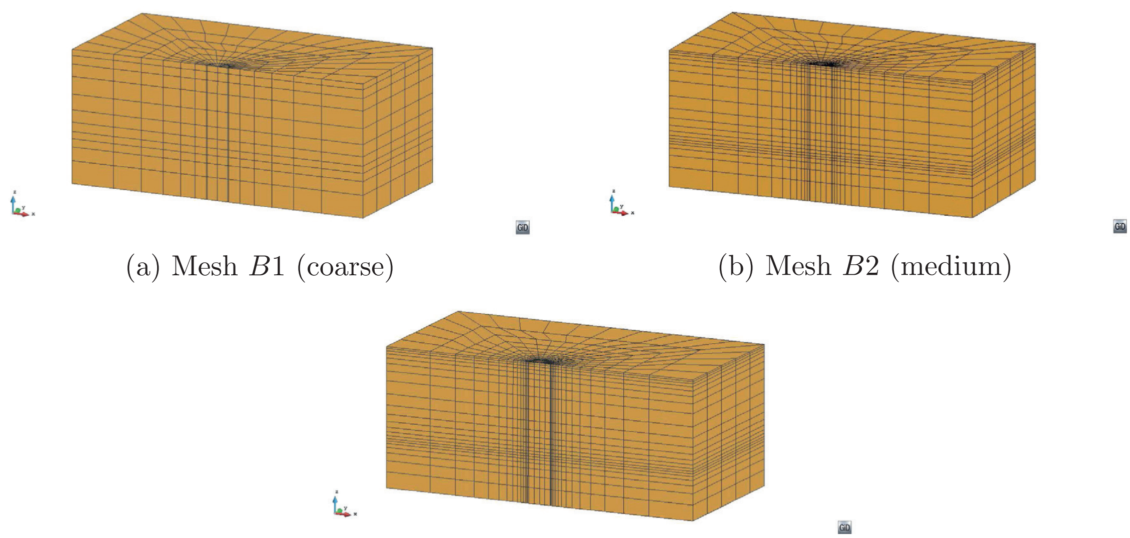

(a) Mesh $B1$ (coarse)

(b) Mesh $B2$ (medium)

(c) Mesh $B3$ (fine)

Fig. 21. FE meshes employed for mesh sensitivity analysis.

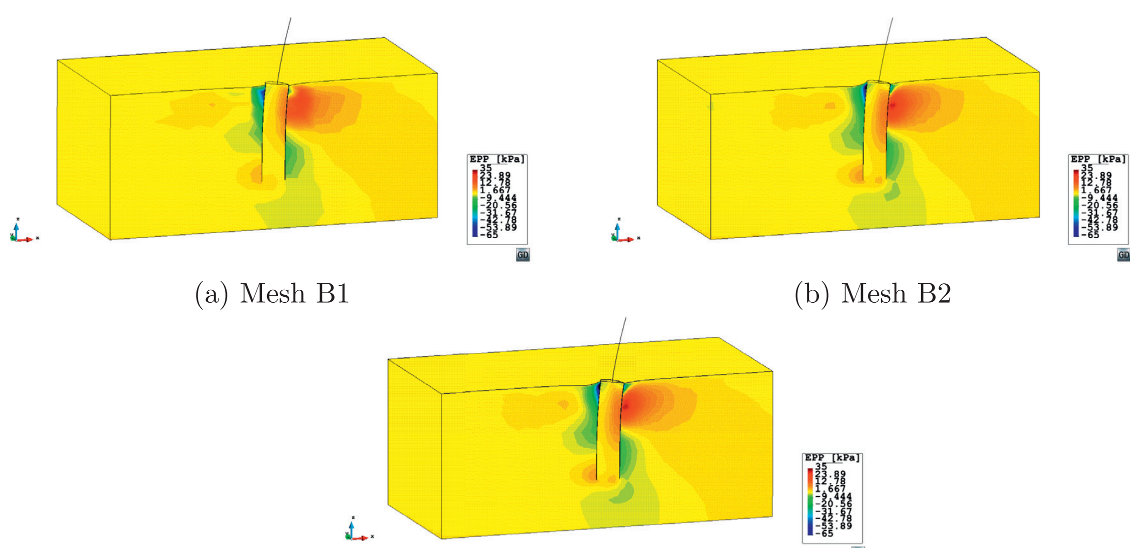

(a) Mesh B1

(b) Mesh B2

(c) Mesh B3

Fig. 22. Mesh sensitivity analysis: excess pore pressure at the second positive load peak (Fig. 4b).

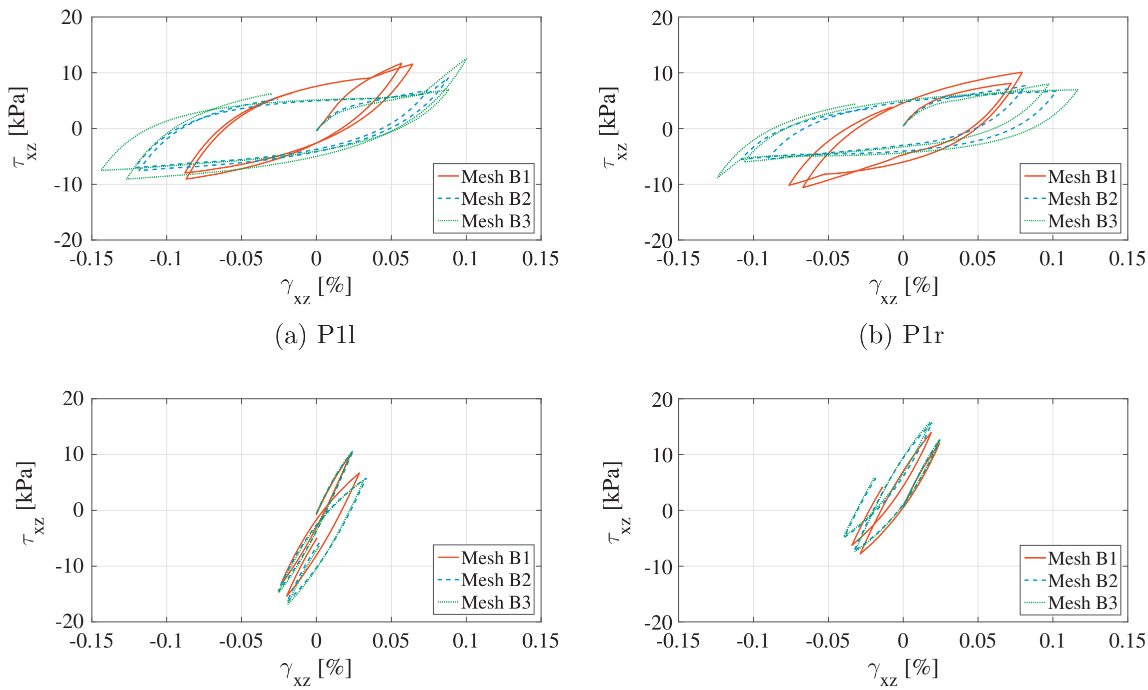

(a) P1l (b) P1r (c) P2l (d) P2r

Fig. 23. Mesh sensitivity analysis: $\tau_{xz} - \gamma_{xz}$ cycles at the four control points in Fig. 17.

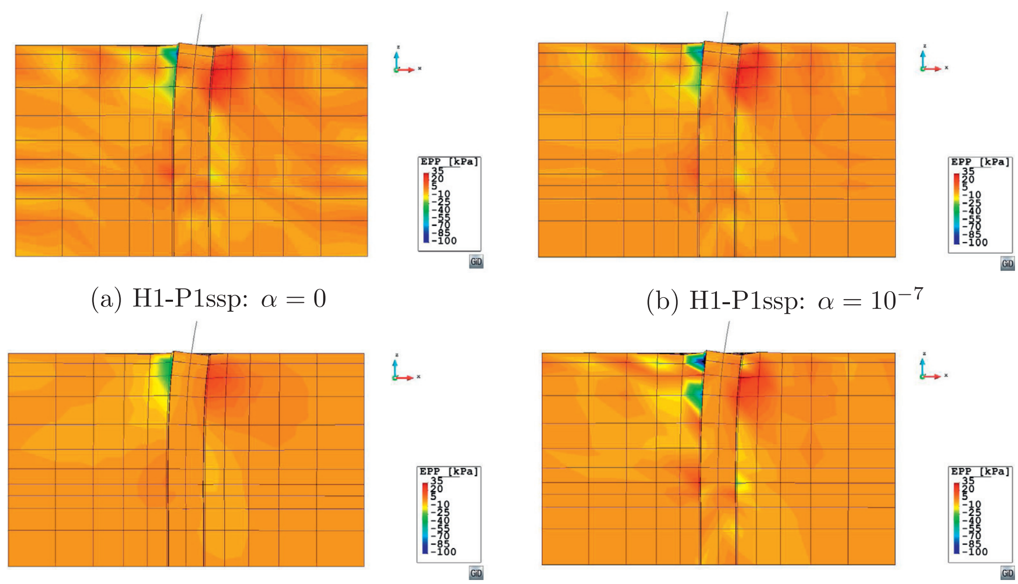

(a) H1-P1ssp: $\alpha = 0$ (b) H1-P1ssp: $\alpha = 10^{-7}$ (c) H1-P1ssp: $\alpha = 10^{-5}$ (d) H1-P1

Fig. 24. Pressure stabilization analysis: excess pore pressure at the first positive load peak (Fig. 4b).

set by Cuéllar et al. [16] for a similar OWT problem. Both in Cuéllar et al. [16] and this study, the seeming coarseness of the adopted meshes is substantially remedied by the use of 8-node elements based on enhanced assumed strain formulations [61,58].

As for time marching, the time-step size Δt = 0.004 s reported in Section 3.4 is 1/10 of the sampling step size in the anemometric records, and fulfils the requirement $\Delta t < \Delta x_{avg}/V_s$ with $\Delta x_{avg} \approx 1$ m and $\Delta V_s \approx 200$ m/s. Further, Krylov-Newton step iterations [75] are arrested when an error criterion on the incremental displacement norm is satisfied with relative tolerance equal to 7.5×10^{-4} [56]. Although smaller time-steps may suit better the integration of highly non-linear soil models [38,82], the selection of Δt (and of the error tolerance) is largely driven by computational cost arguments.

A.3. Pore pressure stabilisation

The effect of the stabilization parameter α in Eq. (2) is illustrated in Fig. 24 for the same analysis case in Fig. 17. The excess pore pressure contour plots at the first positive load peak (Fig. 17b) are reported for the following four cases, all analysed through the coarse mesh A (Fig. 18a) for computational convenience: (i) H1-P1ssp elements with inhibited stabilization ($\alpha = 0$); (ii) H1-P1ssp elements stabilised with a low α value ($\alpha = 10^{-7}$); (iii) H1-P1ssp elements and $\alpha = 10^{-5}$ (from Eq. (3)); (iv) standard H1-P1 elements (no stabilisation).

Checkerboard pressure patterns are apparent in Fig. 24a and d (no stabilisation) and, to a lesser extent, in Fig. 24b as well, where $\alpha = 10^{-7}$ proves still too low for satisfactory stabilisation. Conversely, a smooth pore pressure field results when $\alpha = 10^{-5}$ is calibrated through Eq. (3) (Fig. 24c), with pressure amplitudes overall comparable to the other unsatisfactory cases. The final value $\alpha = 6 \times 10^{-6} < 10^{-5}$ used in the main simulations (Section 3.4) has been determined to comply with Eq. (3) in presence of the finer mesh B2 (Fig. 21b).

References

[1] Abdel-Rahman K, Achmus M. Finite element modelling of horizontally loaded monopile foundations for offshore wind energy converters in Germany. In: Proceedings of the international symposium on frontiers in offshore geotechnics, Perth, WA, Australia. p. 391–6.
[2] Achmus M, Kuo Y-S, Abdel-Rahman K. Behavior of monopile foundations under cyclic lateral load. Comput Geotech 2009;36(5):725–35.
[3] Arany L, Bhattacharya S, Macdonald JHG, Hogan SJ. Closed form solution of eigenfrequency of monopile supported offshore wind turbines in deeper waters incorporating stiffness of substructure and SSI. Comput Geotech 2016;83:18–32.
[4] Arapogianni A, Genachte A-B, et al. Deep water: the next step for offshore wind energy Technical report. Brussels (Belgium): European Wind Energy Association; 2013.
[5] Babuška I. The finite element method with Lagrangian multipliers. Numer Math 1973;20(3):179–92.
[6] Bhattacharya S, Cox JA, Lombardi D, Wood DM. Dynamics of offshore wind turbines supported on two foundations. Proc Inst Civ Eng: Geotech Eng 2013;166:159–69.
[7] Bienen B, Dührkop J, Grabe J, Randolph MF, White DJ. Response of piles with wings to monotonic and cyclic lateral loading in sand. J Geotech Geoenviron Eng 2011;138(3):364–75.
[8] Bonilla LF, Archuleta RJ, Lavallée D. Hysteretic and dilatant behavior of cohesionless soils and their effects on nonlinear site response: field data observations and modeling. Bull Seismol Soc Am 2005;95(6):2373–95.
[9] Brezzi F. On the existence, uniqueness and approximation of saddle-point problems arising from Lagrangian multipliers. Rev fr d'autom inf rech opér Anal num 1974;8(2):129–51.
[10] Byrne BW, McAdam RA, Burd HJ, Houlsby GT, Martin CM, Gavin K, et al. Field testing of large diameter piles under lateral loading for offshore wind applications. In: Proceedings of the 16th European conference on soil mechanics and geotechnical engineering, Edinburgh, UK. p. 1255–60.
[11] Byrne BW, McAdam RA, Burd HJ, Houlsby GT, Martin CM, Zdravković L, et al. New design methods for large diameter piles under lateral loading for offshore wind applications. In: Proceedings of 3rd international symposium on frontiers in offshore geotechnics, Oslo, Norway. p. 705–10.
[12] Cheng Z, Jeremić B. Numerical modeling and simulations of piles in liquefiable soil. Soil Dyn Earthq Eng 2009;29(11–12):1405–16.
[13] Chopra AK. Dynamics of structures, vol. 3. New Jersey: Prentice Hall; 1995.
[14] Corti R, Diambra A, Wood DM, Escribano DE, Nash DF. Memory surface hardening model for granular soils under repeated loading conditions. J Eng Mech 2016:04016102.
[15] Cuéllar P. Pile foundations for offshore wind turbines: numerical and experimental investigations on the behaviour under short-term and long-term cyclic loading. PhD thesis, Technischen Universität Berlin; 2011.
[16] Cuéllar P, Mira P, Pastor M, Fernández-Merodo JA, Baeßler M, Rücker W. A numerical model for the transient analysis of offshore foundations under cyclic loading. Comput Geotech 2014;59:75–86.
[17] Dafalias YF, Manzari MT. Simple plasticity sand model accounting for fabric change effects. J Eng Mech 2004;130(6):622–34.
[18] Damgaard M, Bayat M, Andersen LV, Ibsen LB. Assessment of the dynamic behaviour of saturated soil subjected to cyclic loading from offshore monopile wind turbine foundations. Comput Geotech 2014;61:116–26.
[19] De Borst R, Crisfield MA, Remmers JJ, Verhoosel CV. Nonlinear finite element analysis of solids and structures. John Wiley & Sons; 2012.
[20] di Prisco CG, Mortara G. A multi-mechanism constitutive model for plastic adaption under cyclic loading. Int J Numer Anal Methods Geomech 2013;37:3071–86.
[21] di Prisco CG, Wood DM. Mechanical behaviour of soils under environmentally-induced cyclic loads. Springer; 2012.
[22] Doherty P, Gavin K. Laterally loaded monopile design for offshore wind farms. Proc Inst Civ Eng – Energy 2012;165(1):7–17.
[23] Elgamal A, Lu J. A framework for 3D finite element analysis of lateral pile system response. In: Proceedings of the international foundation congress and equipment expo, Orlando, Florida, USA. ASCE; 2009. p. 616–23.
[24] Elgamal A, Lu J, Forcellini D. Mitigation of liquefaction-induced lateral deformation in a sloping stratum: three-dimensional numerical simulation. ASCE J Geotech Geoenviron Eng 2009;135(11):1672–82.
[25] Elgamal A, Yang Z, Lai T, Kutter BL, Wilson DW. Dynamic response of saturated dense sand in laminated centrifuge container. J Geotech Geoenviron Eng 2005;131(5):598–609.
[26] Elgamal A, Yang Z, Parra E, Ragheb A. Modeling of cyclic mobility in saturated cohesionless soils. Int J Plasticity 2003;19(6):883–905.
[27] Foti S, Lai CG, Lancellotta R. Porosity of fluid-saturated porous media from measured seismic wave velocities. Géotechnique 2002;52:359–73.
[28] Gazzo A, Matzen F, Farhangi C, Lamdaouar A. Offshore wind in Europe – walking the tightrope to success Technical report. London (UK): Ernst & Young; 2015.
[29] Griffiths DV. Numerical modeling of interfaces using conventional finite elements. In: Proceedings of 5th international conference on numerical methods in geomechanics, Nagoya, Japan. p. 837–44.
[30] Hasselmann K, Barnett TP, Bouws E, Carlson H, Cartwright DE, Enke K, et al. Measurements of wind-wave growth and swell decay during the Joint North Sea Wave Project (JONSWAP) Technical report. Hamburg (Germany): Deutches Hydrographisches Institut; 1973.
[31] Hsu SA, Meindl EA, Gilhousen DB. Determining the power-law wind-profile exponent under near-neutral stability conditions at sea. J Appl Meteorol 1994;33(6):757–65.
[32] Huang M, Yue ZQ, Tham LG, Zienkiewicz OC. On the stable finite element procedures for dynamic problems of saturated porous media. Int J Numer Methods Eng 2004;61(9):1421–50.
[33] Huang NE, Long SR, Tung CC, Yuen Y, Bliven LF. A unified two-parameter wave spectral model for a general sea state. J Fluid Mech 1981;112:203–24.
[34] Hughes TJR. The finite element method: linear static and dynamic finite element analysis. Prentice-Hall; 1987.
[35] Iai S, Morita T, Kameoka T, Matsunaga Y, Abiko K. Response of a dense sand deposit during 1993 Kushiro-oki earthquake. Soils Found – Jpn Soc Soil Mech Found Eng 1995;35(1):115–31.
[36] Ishihara K, Tatsuoka F, Yasuda S. Undrained deformation and liquefaction of sand under cyclic stresses. Soils Found – Jpn Soc Soil Mech Found Eng 1975;15(1):29–44.
[37] Jeremić B, Cheng Z, Taiebat M, Dafalias YF. Numerical simulation of fully saturated porous materials. Int J Numer Anal Methods Geomech 2008;32(13):1635–60.
[38] Jeremić B, Jie G, Preisig M, Tafazzoli N. Time domain simulation of soil–foundation–structure interaction in non–uniform soils. Earthq Eng Struct Dyn 2009;38(5):699–718.
[39] Jonkman JM, Butterfield S, Musial W, Scott G. Definition of a 5-MW reference wind turbine for offshore system development Technical report. Golden (Colorado, USA): National Renewable Energy Laboratory (NREL); 2009.
[40] Journée JMJ, Massie WW. Offshore hydromechanics. TU Delft; 2000.
[41] Kallehave D, Byrne BW, Thilsted CL, Mikkelsen KK. Optimization of monopiles for offshore wind turbines. Philos Trans Roy Soc Lond A: Math Phys Eng Sci 2015;373(2035):1–15.
[42] Kallehave D, Thilsted CL, Liingaard M. Modification of the API p-y formulation of initial stiffness of sand. In: Proceedings of offshore site investigation and geotechnics: integrated technologies – present and future, London, UK. Society of Underwater Technology; 2012. p. 465–72.
[43] Kramer SL. Geotechnical earthquake engineering, vol. 80. Upper Saddle River (NJ): Prentice Hall; 1996.
[44] Kühn MJ. Dynamics and design optimisation of offshore wind energy conversion systems. Delft University of Technology; 2001.
[45] van Kuik GAM, Peinke J, Nijssen R, Lekou DJ, Mann J, Sørensen JN, et al. Long-term research challenges in wind energy – a research agenda by the European Academy of Wind Energy. Wind Energy Sci 2016;1:1–39.
[46] Lade PV, Duncan JM. Elastoplastic stress-strain theory for cohesionless soil. J Geotech Eng Div 1975;101(10):1037–53.
[47] Lanzafame R, Messina M. Fluid dynamics wind turbine design: critical analysis, optimization and application of BEM theory. Renew Energy 2007;32(14):2291–305.
[48] LeBlanc C, Houlsby GT, Byrne BW. Response of stiff piles in sand to long-term cyclic lateral loading. Géotechnique 2010;60(2):79–90.
[49] Lombardi D, Bhattacharya S, Wood DM. Dynamic soil–structure interaction of monopile supported wind turbines in cohesive soil. Soil Dyn Earthq Eng 2013;49:165–80.
[50] López-Querol S, Fernández-Merodo JA, Mira P, Pastor M. Numerical modelling of dynamic consolidation on granular soils. Int J Numer Anal Methods Geomech 2008;32(12):1431–57.
[51] Lu J, Elgamal A, Yang Z. OpenSeesPL: 3D lateral pile-ground interaction. San Diego: University of California; 2011.
[52] Lysmer J, Kuhlemeyer RL. Finite dynamic model for infinite media. J Eng Mech Div 1969;95(4):859–78.
[53] Madsen HA, Bak C, Døssing M, Mikkelsen R, Øye S. Validation and modification of the blade element momentum theory based on comparisons with actuator disc simulations. Wind Energy 2010;13(4):373–89.

[54] Manwell JF, McGowan JG, Rogers AL. Wind energy explained: theory, design and application. John Wiley & Sons; 2010.
[55] Masters I, Chapman JC, Willis MR, Orme JAC. A robust blade element momentum theory model for tidal stream turbines including tip and hub loss corrections. J Mar Eng Technol 2014;10(1):25–35.
[56] Mazzoni S, McKenna F, Scott M, Fenves G. OpenSees command language manual; 2007.
[57] McGann CR, Arduino P, Mackenzie-Helnwein P. Stabilized single-point 4-node quadrilateral element for dynamic analysis of fluid saturated porous media. Acta Geotech 2012;7(4):297–311.
[58] McGann CR, Arduino P, Mackenzie-Helnwein P. A stabilized single-point finite element formulation for three-dimensional dynamic analysis of saturated soils. Comput Geotech 2015;66:126–41.
[59] McKenna FT. Object-oriented finite element programming: frameworks for analysis, algorithms and parallel computing. Berkeley: University of California; 1997.
[60] Melendo A, Coll A, Pasenau M, Escolano E, Monros A. <http://www.gidhome.com>; 2015 [Online; accessed Nov-2015].
[61] Mira P, Pastor M, Li T, Liu X. A new stabilized enhanced strain element with equal order of interpolation for soil consolidation problems. Comput Methods Appl Mech Eng 2003;192(37):4257–77.
[62] Moriarty PJ, Hansen AC. AeroDyn theory manual Technical report. Golden (Colorado, USA): National Renewable Energy Laboratory (NREL); 2005.
[63] Morison JR, O'Brien MP, Johnson JW, Schaaf SA. The force exerted by surface waves on piles. J Petrol Technol 1950;2(05):149–54.
[64] Mróz Z, Norris VA, Zienkiewicz OC. An anisotropic hardening model for soils and its application to cyclic loading. Int J Numer Anal Methods Geomech 1978;2:203–21.
[65] Newman JN. Marine hydrodynamics. MIT press; 1977.
[66] Ochi MK, Hubble EN. Six-parameter wave spectra. Coast Eng Proc 1976;1(15):301–28.
[67] Panofsky HA, Dutton JA. Atmospheric turbulence: models and methods for engineering applications. John Wiley & Sons; 1984.
[68] Pierson WJ, Moskowitz L. A proposed spectral formulation for fully developed wind seas based on the similarity theory of S.A. Kitaigorodskii. J Geophys Res 1964;69(24):5181–90.
[69] Pisanò F, Jeremić B. Simulating stiffness degradation and damping in soils via a simple visco-elastic–plastic model. Soil Dyn Earthq Eng 2014;63:98–109.
[70] Preisig M, Prévost JH. Stabilization procedures in coupled poromechanics problems: a critical assessment. Int J Numer Anal Methods Geomech 2011;35(11):1207–25.
[71] Prévost JH. A simple plasticity theory for frictional cohesionless soils. Int J Soil Dyn Earthq Eng 1985;4(1):9–17.
[72] Prévost JH, Popescu R. Constitutive relations for soil materials. Electron J Geotech Eng 1996.
[73] Roten D, Fäh D, Bonilla LF. High-frequency ground motion amplification during the 2011 Tohoku earthquake explained by soil dilatancy. Geophys J Int 2013;193(2):898–904.
[74] Rudolph C, Bienen B, Grabe J. Effect of variation of the loading direction on the displacement accumulation of large-diameter piles under cyclic lateral loading in sand. Can Geotech J 2014;51(10):1196–206.
[75] Scott MH, Fenves GL. A Krylov subspace accelerated Newton algorithm. In: Proceedings of 2003 ASCE structures congress, Seattle, Washington, USA.
[76] Sloan SW. Substepping schemes for the numerical integration of elastoplastic stress–strain relations. Int J Numer Methods Eng 1987;24(5):893–911.
[77] Thieken K, Achmus M, Lemke K. Evaluation of a new p-y approach for piles in sand with arbitrary dimensions. In: Proceedings of 3rd international symposium on frontiers in offshore geotechnics, Oslo, Norway. p. 705–10.
[78] Thieken K, Achmus M, Lemke K. A new static p-y approach for piles with arbitrary dimensions in sand. Geotechnik 2015;38(4):267–88.
[79] van der Tempel J. Design of support structures for offshore wind turbines PhD thesis. Technische Universiteit Delft; 2006.
[80] Versteijlen WG, Metrikine AV, van Dalen KN. A method for identification of an effective winkler foundation for large-diameter offshore wind turbine support structures based on in-situ measured small-strain soil response and 3D modelling. Eng Struct 2016.
[81] Vugts JH, van der Tempel J, Schrama EA. Hydrodynamic loading on monotower support structures for preliminary design. In: Proceedings of offshore wind energy EWEA special topic conference, Brussels, Belgium.
[82] Watanabe K, Pisanò F, Jeremić B. Discretization effects in the finite element simulation of seismic waves in elastic and elastic-plastic media. Eng Comput 2016:1–27.
[83] Yang Z, Elgamal A. Multi-surface cyclic plasticity sand model with lode angle effect. Geotech Geol Eng 2008;26(3):335–48.
[84] Yang Z, Elgamal A, Parra E. Computational model for cyclic mobility and associated shear deformation. J Geotech Geoenviron Eng 2003;129(12):1119–27.
[85] Zdravković L, Taborda DMG, Potts DM, Jardine RJ, Sideri M, Schroeder FC, et al. Numerical modelling of large diameter piles under lateral loading for offshore wind applications. In: Proceedings of 3rd international symposium on frontiers in offshore geotechnics, Oslo, Norway.
[86] Zienkiewicz OC, Chan AHC, Pastor M, Schrefler BA, Shiomi T. Computational geomechanics. Chichester: Wiley; 1999.
[87] Zienkiewicz OC, Chang CT, Bettess P. Drained, undrained, consolidating and dynamic behaviour assumptions in soils. Géotechnique 1980;30(4):385–95.
[88] Zienkiewicz OC, Shiomi T. Dynamic behaviour of saturated porous media; the generalized Biot formulation and its numerical solution. Int J Numer Anal Methods Geomech 1984;8(1):71–96.